



Dynamically Pulsed Catalysis for Selective Ammonia Synthesis

A Major Qualifying Project
Submitted to the Faculty of
Worcester Polytechnic Institute
In partial fulfilment of the requirements
For the degree in Bachelor's of Science
In
Chemical Engineering

By
Avery Cirincione-Lynch
Eileen Piombino

Date: April 28, 2022

Project Advisor: Professor Andrew Teixeira (CHE)

This report represents the work of WPI undergraduate students submitted to the faculty as evidence of a degree requirement. WPI routinely publishes these reports on its website without editorial or peer review. For more information about the projects program at WPI, see <http://www.wpi.edu/Academics/Projects>

Abstract

Ammonia is one of the most highly demanded chemicals globally, with applications ranging from agriculture to everyday cleaning products. The industrial process of producing ammonia from elemental nitrogen and hydrogen, known as the Haber-Bosch process, is highly inefficient, requiring high temperatures and pressures for relatively low conversions of the reaction. Recent work has shown that dynamically oscillated operating conditions may enhance the catalytic effect of heterogeneous catalytic reactions, similar to the industrial method of ammonia synthesis. Based on published research, we propose that sufficiently fast thermal oscillations of a catalyst surface will increase the efficiency of ammonia synthesis catalysis, achieving higher reaction conversion rates at milder, more energetically favorable operating conditions. Here, we present the design and fabrication of a microreactor for investigation into the theoretical and experimental capabilities of thermally pulsed catalysis for selective ammonia synthesis. By resistively heating a thin platinum catalyst on an aluminum nitride substrate, integrating a cooling system, and incorporating an ultrafast pyrometer for millisecond temperature monitoring and control, we achieved thermal oscillations close to the desired timescale for pulsed catalysis. Finally, we suggest several design improvements to make this system usable for the direct analysis of pulsed heterogeneous catalysis.

Acknowledgements

Firstly, the team would like to thank our advisor, Professor Andrew R. Teixeira, PhD, who has led our team through this project. Professor Teixeira has challenged us to meet a standard of excellence, think critically and creatively, and develop professionally. We are incredibly thankful for his support and advice throughout the past 14 months. We would also like to thank the graduate students working in the Teixeira Research Lab, especially PhD student Cameron Armstrong, who provided us daily support from helping us get used to finding our way around the lab to making sense of experimental phenomena. In addition, we would like to recognize the chemical engineering department's electronics engineer Douglas White and advanced machinist Ian Anderson, who provided invaluable help in modifying our reactor chuck, fabricating our substrates, and troubleshooting the (many) complications that arose throughout this project. Finally, our team would like to give credit to Armela Xhindole, who used CAD to produce diagrams of the initial design of the reactor, which the team used as a basis for this project and in the design considerations section of this paper to present the preliminary designs of the reactor.

Table of Contents

Abstract.....	iii
Acknowledgements.....	iv
Table of Contents.....	v
List of Figures.....	vii
List of Tables.....	ix
1.0 Introduction.....	1
2.0 Background.....	2
2.1 Technical Considerations.....	2
2.1.1 Ammonia Synthesis & Heterogeneous Catalysis.....	2
2.1.2 Catalytic Turnover & Optimization.....	4
2.2 Microreactor Design Considerations.....	5
2.2.1 First Iteration: Preliminary Design.....	5
2.2.2 Second Iteration: Temperature Monitoring for Control Considerations.....	5
2.2.3 Third Iteration: Cooling Considerations.....	7
2.2.4 Substrate Material Selection.....	7
3.0 Methodology.....	8
3.1 Computational Heat Transfer Model.....	8
3.2 Proof of Theory.....	9
3.2.1 Pyrometer Performance/Calibration.....	9
3.2.2 Proof of Heating.....	10
3.2.3 Temperature Control Loop.....	11
3.3 Final Reactor Fabrication and Testing.....	12
3.3.1 Experimental Design.....	12
3.3.2 AlN Chip Fabrication.....	12
3.3.3 Reactor Heating Tests.....	13
3.3.4 Reactor Cooling Tests.....	14
3.3.5 Temperature-Controlled Square Wave Tests.....	14
3.3.6 Reactor Sealing Tests.....	15
4.0 Results and Discussion.....	16
5.1 Reactor Fabrication.....	16

5.2 Computational Heat Transfer Modeling	16
5.3 Proof of Theory	17
5.3.1 Pyrometer Performance/Calibration	17
5.3.2 Proof of Heating.....	18
5.3.3 Temperature Control Loop	18
5.4 Final Reactor Fabrication and Tests	20
5.4.1 AlN Chip Fabrication.....	20
5.4.2 Voltage Heating Tests.....	21
5.4.3 Reactor Cooling Tests.....	22
5.4.4 Temperature-Controlled Square Wave Tests.....	23
5.0 Conclusion	26
6.0 Future Recommendations	26
6.1 Short-Term Future Recommendations.....	26
6.1.1 Catalyst Deposition.....	26
6.1.2 Reactor Sealing	26
6.1.3 Additional Short-Term Considerations.....	27
6.2 Medium-Term Recommendations	27
6.2.1 Heating Rate Enhancements	27
6.2.2 Cooling Rate Enhancements	27
6.3 Long-Term Recommendations	28
6.3.1 Chemical Compatibility	28
6.3.2 On-Demand Chemical Manufacturing.....	28
Appendix A: Final Reactor Component Table	29
Appendix B: Voltage Heating Complete Data.....	30
Appendix C: Cooling Time and Rate Data	31
References.....	32

List of Figures

Figure	Page
Figure 1: Concentration of ammonia at equilibrium for various T and P conditions. ¹⁰	2
Figure 2: Computationally modeled free energy reaction pathways for elementary steps of ammonia synthesis on a heterogeneous catalyst. ¹⁶	3
Figure 3: Configuration of the microreactor parts. In order from the bottom, there is aluminum reactor base, the substrate with the aluminum strip (red), the gold contacts (gold), the gasket, then the aluminum reactor lid. The tubes shown in the figure are the gas inlet and outlet tubes.	5
Figure 4: Path of pyrometer infrared laser. Includes the spot size at the sensor head as well as at the distance from the surface under inspection.	6
Figure 5: Graphic of window overlaid on the gasket. Includes proposed dimensions.	6
Figure 6: 2-D design schematic for reactor chuck alterations needed to facilitate the inclusion of pyrometer.	6
Figure 7: Experimental setup for pyrometer calibration. Includes thermocouple, multimeter with leads in pyrometer output pins, hotplate, steel slate.....	10
Figure 8: Experimental setup for proof of theory heat tests. Includes reactor, power supply lead, and sense lead configuration.	11
Figure 9: Experimental setup for temperature control tests. Includes steel strip connected to power supply with pyrometer and sense leads connected to pyrometer output.....	12
Figure 10: Final reactor design schematic with N ₂ and H ₂ feed and NH ₃ product stream to a mass spectrometer (MS) for analysis. Here, the sense leads of the power supply are connected to the voltage output of the pyrometer for direct temperature control.....	12
Figure 11: Experimental setup for heating tests. Includes sense leads attached to the copper leads of the reactor, as opposed to the pyrometer output pins as in the temperature-controlled setup.	13
Figure 12: Experimental setup for cooling tests. Includes reactor chuck situated on top of cooling block, pyrometer, and power supply connected to the reactor's leads.....	14

Figure 13: Experimental setup for seal testing. Key setup is gas flow tubes emerging from top of reactor and connecting to existing flow system. Gas inlet is on the left and outlet is on the right-hand side of the reactor respectively.	15
Figure 14: Final fabricated reactor chuck	16
Figure 15: Ideal temperature versus time profile as informed by the power requirements determined through COMSOL.....	16
Figure 16: Plot of temperature measured by pyrometer (blue) and temperature measured by thermocouple (orange) as a function of the output voltage of the pyrometer. Figure includes best fit line for output voltage versus temperature measured by pyrometer..	17
Figure 17: Photograph of fabricated SiO ₂ chip situated in reactor base.....	18
Figure 18: Temperature versus time profile obtained for controlled stepping from room temperature to 200 °C in 20 °C intervals.	18
Figure 19: Temperature versus time profile obtained for controlled heating from room temperature to 75 °C with different current limits.	19
Figure 20: Reactor chip fabricated via initial process (left) and modified process (right).....	21
Figure 21: Temperature versus time profiles obtained from applying a given voltage for 5 seconds for trials with no coolant, 10 mL/min coolant flow, 20 mL/min coolant flow, and 30 mL/min coolant flow. In order from left to right, the peaks observed in the figure correspond to the application of 10 V, 20 V, 30 V, and 40 V respectively.....	21
Figure 22: Square wave temperature oscillations for 100-150 °C, 100-200 °C, 100-250 °C, and 100-300 °C with a 2 s dwell time in each regime.	23
Figure 23: Temperature versus time profile obtained for oscillations between 100-150 °C and between 100-200 °C for a 0.5 s dwell time.....	25

List of Tables

Table	Page
Table 1: Comparison of relevant properties for proposed window materials. Includes dimensions, wavelength range, Knoop hardness, and cost.	7
Table 2: Comparison of common substrates based on thermal conductivity.	8
Table 3: Comparison of narrowed list of substrate options based on electrical resistivity.....	8
Table 4: Predetermined temperatures and dwell times for temperature-controlled square wave tests. The Low-High designation corresponds to the low setpoint and high setpoint between which the oscillations occur with dwell time corresponding to the amount of time in each regime.	15
Table 5: Heating requirements for thermally pulsed temperature regimes based on COMSOL results.	16
Table 6: Precision of pyrometer at different operating temperatures as indicated by the error associated with temperature readings. As shown, as temperature increases, the pyrometer becomes more precise.	17
Table 7: Time to cool and cooling rates for cooling from 300-200°C, 250-100°C, and 200-100°C. For each 100°C increment the resulting times and rates are recorded for no coolant flow, 10mL/min, 20mL/min, and 30mL/min.	22
Table 8: heating times and rates for temperature transitions from a starting temperature, T_1 to predetermined temperature setpoint, T_2 . These trials were conducted with 20 mL/min coolant flow.....	23
Table 9: Overshoot magnitudes and stabilization times for controlled temperature transitions from T_1 to T_2 with 20 mL/min coolant flow.	24

1.0 Introduction

Ammonia is one of the most highly demanded chemicals globally. With applications ranging from agriculture to everyday cleaning products, an estimated 150 million tons of ammonia was produced in 2021 worldwide.¹ Despite the extensive research that has gone into optimizing the prominent industrial-scale ammonia synthesis process known as the Haber-Bosch process, the reaction remains relatively inefficient with only an approximated 10-15% conversion rate. In addition, the reaction is extremely energy-intensive, requiring high pressures, high temperatures, and catalyst maintenance.

In a Department of Energy roundtable discussion in 2016, a panel of field experts were tasked with “exploring the scientific challenges associated with discovering alternative, sustainable processes for ammonia production.”² While the panel agreed that the Haber-Bosch process is reasonably well optimized in terms of traditionally manipulated process variables such as temperature and pressure, it is estimated that ammonia synthesis as it currently stands requires an energy input of approximately 8-12 MWh/ton.³ This makes ammonia synthesis responsible for 1-2% of global energy consumption,⁴ and presents the challenge of how to enhance the energy-efficiency of ammonia synthesis. The development of catalysts and catalytic methodologies that can achieve high selectivity and conversion at mild operating conditions will be critical in overcoming this challenge. Moreover, an increase in reaction efficiency could result in decentralization by making smaller-scale and on-demand production more economical.

Ammonia synthesis is a heterogeneous catalytic reaction, and accordingly progresses through a natural catalytic cycle including adsorption, reaction at the catalytic surface,

and desorption. Generally speaking, the catalytic cycle is typically characterized by competing phenomena wherein different steps are optimized under different and distinct conditions.⁵ As such, conducting heterogeneous catalysis such as ammonia synthesis under static conditions results in one or more steps progressing at a less-than-optimal rate, slowing the overall reaction rate. In recent years, researchers have begun exploring the concept of dynamically oscillated operating conditions as a method of individually optimizing the steps of the catalytic cycle. Moreover, researchers hypothesize that achieving forced oscillations in resonance with the natural frequency of the catalytic cycle may amplify the catalytic turnover rate.⁵ If this theory is confirmed, this amplification could result drastically enhanced conversion, selectivity, and overall throughput.

Recent works have demonstrated enhanced rates of reaction through forced oscillations.⁶ Despite the promise of these results, several limitations inhibit the ability to draw direct correlations between the theory of amplifying catalytic turnover rates and the perceived increase in overall reaction rate. As detailed in a review of the recent advances in dynamically pulsed catalysis, the limitations of exploring thermally pulsed catalysis as outlined in existing published works include both theoretical gaps and experimental limitations.⁵ With regards to the later, fabricating reaction systems capable of producing and sustaining square wave functionality in the desired temperature regimes and at the desired frequencies has emerged as a significant challenge. Additionally, monitoring the temperature of the catalytic surface on the desired timescales has yet to be achieved. With specific focus on producing a reactor chip predicated on catalytic platinum capable of resistive heating,

incorporating cooling to achieve desired heat transfer rates and protect reactor components, and establishing a temperature monitoring and control system, this project explores the fabrication and performance of a microreactor capable of overcoming several existing experimental limitations of thermally pulsed catalysis.

2.0 Background

2.1 Technical Considerations

2.1.1 Ammonia Synthesis & Heterogeneous Catalysis

Throughout the development of the Haber-Bosch process, the discovery of highly active catalysts for the synthesis of ammonia from its elements was of upmost concern.⁷ Initial research by Fritz Haber detected excellent catalytic activity in osmium and uranium-based carbides.⁷ Alwin Mittasch, the first to suggest a multi-component catalyst system, preformed over 20,000 tests of more than 5,000 catalyst systems between 1909 and 1922.⁸ Although catalyst systems for the Haber-Bosch process have undergone much research since that time, the magnetite-based fused iron catalyst proposed by Mittasch's research remains the most commonly employed catalyst in industrial ammonia synthesis.⁹

The overall reaction for the synthesis of ammonia from its elements is shown in Equation 1, with the combination of dinitrogen and dihydrogen producing ammonia and 46.1 kJ of heat per mole of reaction:⁹



Stoichiometrically, this equilibrium reaction implicates four moles on the reactant side of the equation, and only two in the

products. Additionally, heat is produced by the forward reaction (exothermal). Accordingly, Le Chatelier's principle suggests that this reaction's equilibrium will favor the products under high pressure and low temperature. However, due to slow kinetics of the reaction at low temperatures, the Haber-Bosch process is conducted at high temperature and pressure. Unfortunately, this shifts the equilibrium of the reaction towards the decomposition of ammonia, drastically reducing the conversion of reactants. Herein lies the need for highly effective catalysts which can leverage reasonable operating conditions towards the selective and efficient conversion of hydrogen and nitrogen to ammonia.

To optimize ammonia yield, thermodynamic equilibrium as well as kinetic limitations must be considered. Figure 1 illustrates the percentage of ammonia at equilibrium for a variety of temperatures and pressures.¹⁰ When considering the use of a catalyst, it is desirable to attain the maximum theoretical yield at low temperature based on the limit imposed by the thermodynamic equilibrium. But despite the large conversions possible at low temperatures, slow kinetics at these conditions make such conversions impossible to achieve.

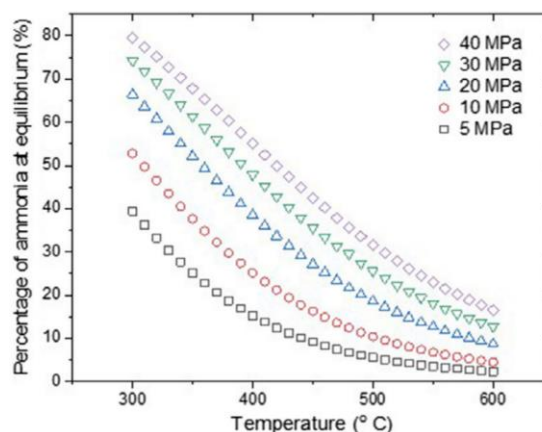


Figure 1: Concentration of ammonia at equilibrium for various T and P conditions.¹⁰

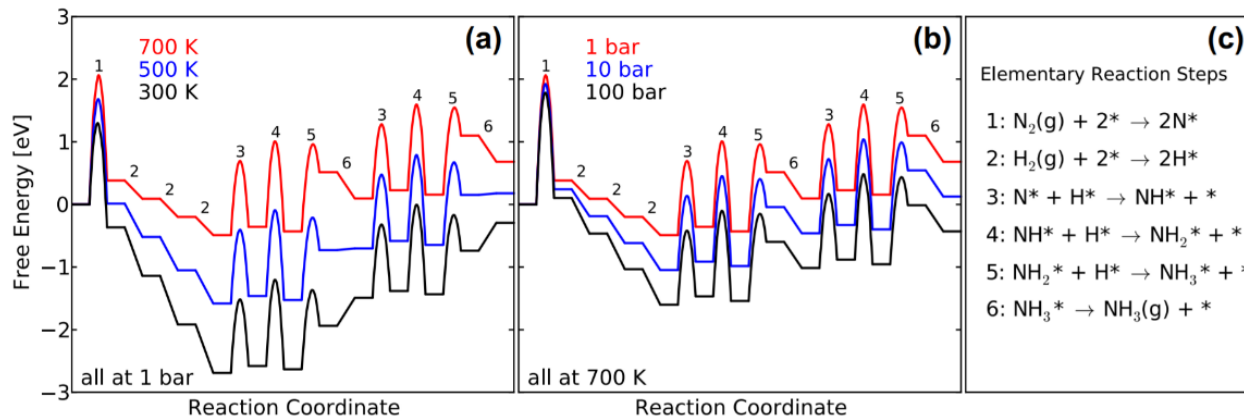
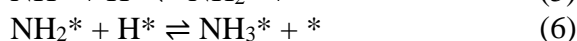


Figure 2: Computationally modeled free energy reaction pathways for elementary steps of ammonia synthesis on a heterogeneous catalyst.¹⁶

For a single pass of the ammonia synthesis loop in most modern Haber-Bosch systems, the conversion rate is limited at around 10-15%. With these systems operating at around 425-450 °C and at pressures above 100 atm, catalysts that could leverage increased reaction rates at lower temperatures would drastically increase the per pass conversion while reducing heating requirements.⁹

The catalytic method most relevant to the industrial synthesis of ammonia (and most relevant to the catalytic technique evaluated in this paper) is heterogeneous catalysis. Specifically, the synthesis of ammonia is catalyzed by the chemisorption of hydrogen and nitrogen on the catalyst surface.⁹ As suggested by Stoltze and Nørskov,¹¹ the synthesis of ammonia via heterogeneous catalysis involves seven proposed mechanistic steps (* denoting a free surface site, and X* representing an adsorbed X atom):^{11,12}



Based on experimentation by Stoltze and Nørskov, as well as further surface science experiments and more recent first-principles calculations, it is widely accepted that the rate-limiting step in this reaction model is the dissociative adsorption of dinitrogen onto the catalyst surface (Eq. 3).^{9,11,13,14} However, researchers such as Ertl and Spencer have suggested that a more comprehensive model is necessary to explain the reaction's kinetic activity, especially when considering the reaction across wider ranges of temperature and pressure.^{12,15} For example, Figure 2¹⁶ illustrates calculated free energy for the synthesis of ammonia on a Ru catalyst for a variety of conditions.

As shown in Figure 2, the reaction follows a Langmuir-Hinshelwood mechanism where both hydrogen and nitrogen undergo dissociative adsorption onto the catalyst surface before the reductive hydrogenation of nitrogen.¹⁴ Each step obeys microscopic reversibility, and thus all steps after the rate-limiting dinitrogen dissociation remain in equilibrium.¹³ Considering the reaction at 300 K and 1 bar (Figure 2a) the reaction remains exergonic and favored by equilibrium, but the increased stability of adsorbed N, NH, and NH₂ on the catalyst surface prevents the reaction from proceeding.¹⁶ When the

temperature is increased to 700 K, the stability of intermediates becomes a lesser constraint, but the overall reaction becomes uphill in free energy, requiring a significant increase in pressure for equilibrium to favor synthesis (Figure 2b).¹⁶ These relationships can be used to clarify what must be taken into account when attempting to choose an effective catalyst, as well as the fundamental drawbacks of traditional catalytic methods.

2.1.2 Catalytic Turnover & Optimization

It is clear from Figure 2a that the harsh conditions used in Haber-Bosh process are not a thermodynamic requirement but are an attempt to leverage the catalytic activity kinetically promoted by high temperature, along with high pressure to promote a productive equilibrium in driving the reaction forward. Therefore, an ideal catalyst would aid in reducing the barrier for N₂ dissociation while maintaining much weaker bonds with the absorbed species. The Brønsted–Evans–Polanyi (BEP) relation describes, for an exothermic reaction, a linear relationship between change in activation energy (E_a) and corresponding change in heat of reaction (ΔH_r).¹⁷

$$E_a = E_a^0 + \alpha \Delta H_r \quad (9)$$

The correlation factor, α , describing the linearity of this relation, is dependent upon the specific the rate limiting mechanism under study, such as surface interactions. DFT calculations have corroborated the applicability of this model for ammonia synthesis.¹⁸

Based on this BEP relation, the catalytic activity of a heterogeneous catalyst, defined as the turnover frequency (TOF) or number of turnovers of a catalytic cycle at an active site per unit time, is optimized at the

intersection of two competing phenomena: absorption of reactants (the slowest kinetic step) and desorption of products (determining the availability of free sites on the catalyst surface).¹⁸ This theoretical maximum of catalytic activity, which balances competing kinetic and thermodynamic factors, is commonly referred to as the Balandin-Sabatier maximum.¹⁹ However, many methods to overcome the Sabatier maximum have been proposed in literature, such as dynamically pulsed catalysis.⁵

The strategy of pulsed catalysis aims to decouple competing reaction phenomena by inducing rapid changes in operating conditions. By disassociating sequential chemistries, distinct reaction phenomena can be enhanced by targeted operating regimes within a single catalytic cycle. Recent theoretical work in dynamic catalysis indicate how catalytic surface dynamics can be leveraged to increase catalytic turnover beyond the Sabatier maximum.^{19,20} One condition that has shown promise for pulsed catalysis is temperature. In research published by Stolte and colleagues, experimental demonstrated that heating a platinum catalyst by pulsing it with 300 mJ of energy at a frequency of 20 Hz resulted in up to 5 times greater conversion when compared to isothermal operation at corresponding conditions.⁶ As detailed in a review of the recent advances in dynamically pulsed catalysis, the limitations of existing published works in pulsed catalysis include both theoretical gaps and experimental limitations.⁵ With regards to the later, fabricating reaction systems capable of producing and sustaining square wave functionality in the desired temperature regimes and at the desired frequencies has emerged as a significant challenge. Additionally, monitoring the temperature of the catalytic surface on the desired timescales has yet to be achieved.

For example, in the previously discussed experiments conducted by Stolte and colleagues, a catalytic surface is pulsed with energy to induce heating. While the energy input is described as a square wave application of energy with a given frequency, the experimental methods do not monitor the corresponding temperature changes of the catalytic surface. As a result, the temperature of the catalytic surface is unlikely to provide the same square wave profile as the energy input, but moreover remains completely uncharacterized. This drastically limits the ability of these tests to draw any conclusions regarding the improvements of catalytic turnover rate in response to temperature oscillations.

2.2 Microreactor Design Considerations

2.2.1 First Iteration: Preliminary Design

The reactor design proposed in this report was inspired by an original design from Stolte and coworkers.⁶ In initial iterations of the design, the team specified dimensions for an aluminum reactor block, a substrate chip, and a gasket that, when configured, form a reaction chamber that allows the flow of a gas feed over a platinum catalyst strip. In this reactor design, an aluminum base supports a reactor chip. Aluminum was selected due to its ease of fabrication and fast heat transfer. The base includes a machined ridge for the reactor chip to be recessed into.

On the proposed reactor chip, a substrate serves as the support for a platinum catalyst as well as gold contacts. These design specifications facilitate temperature alterations of the catalytic surface through resistive heating. Finally, the initial design calls for a gasket sized to place between the reactor chip and the reactor lid. This allows a simple bolting

mechanism to supply the pressure needed to create an airtight seal, which promotes efficient flow of the gas into the reactor chamber through gas inlet tubes. The configuration of the aluminum chuck, gasket, and substrate are given in the figure below.

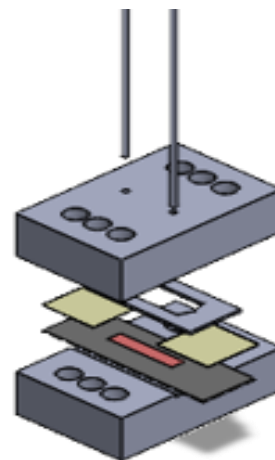


Figure 3: Configuration of the microreactor parts. In order from the bottom, there is aluminum reactor base, the substrate with the aluminum strip (red), the gold contacts (gold), the gasket, then the aluminum reactor lid. The tubes shown in the figure are the gas inlet and outlet tubes.

2.2.2 Second Iteration: Temperature Monitoring for Control Considerations

To accurately measure the oscillating temperature of the platinum strip during testing, the design of the reactor was altered to include a pyrometer. The pyrometer, which is an Optris CTLaser 4ML with the CF1 optical specifications of 10:1, has an exposure time of 90 μs , a response time of 300 μs , and a spectral range of 2.2-6 μm . This pyrometer is suited to operate between of 0 °C and 500 °C. This makes the pyrometer a viable option for determining the temperature of the platinum based on the infrared emission spectra within this temperature range.

According to the pyrometer datasheet, the pyrometer specifications allow for a spot size with a diameter of 5 mm when placed 50 mm above the substrate. To incorporate the pyrometer, the second iteration of the design includes a tapped and threaded 10mm diameter circle at the center of the reactor lid. This threading is compatible with a sighting tube and pipe adapter supplied by Optris, which screws into the tapped hole until it is situated 50 mm above the catalytic surface per the pyrometer requirements. The image below was obtained from the online manufacturer's website, and depicts the laser path and spot size of this model pyrometer.

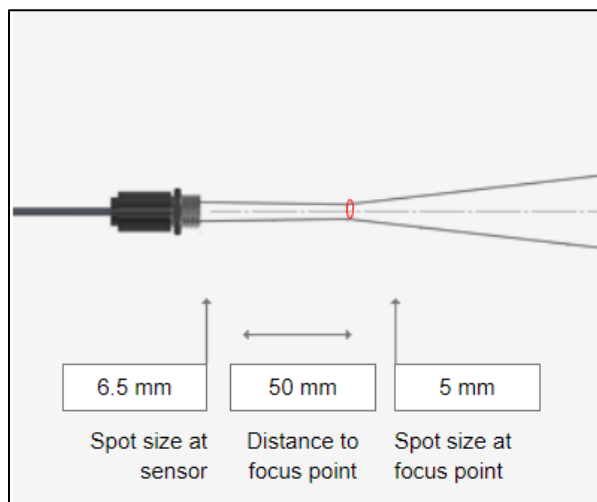


Figure 4: Path of pyrometer infrared laser. Includes the spot size at the sensor head as well as at the distance from the surface under inspection.

In addition, the design includes a machined 12×12 mm on the underside of the reactor lid wherein a window can be recessed. Pressure to seal the window is then applied from the same gasket that seals the reaction chamber. The figures below depict the proposed window overlaid on the gasket and a schematic of the configuration of the reactor chuck with the pyrometer alterations.

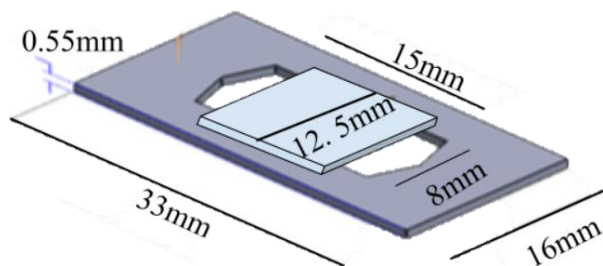


Figure 5: Graphic of window overlaid on the gasket. Includes proposed dimensions.

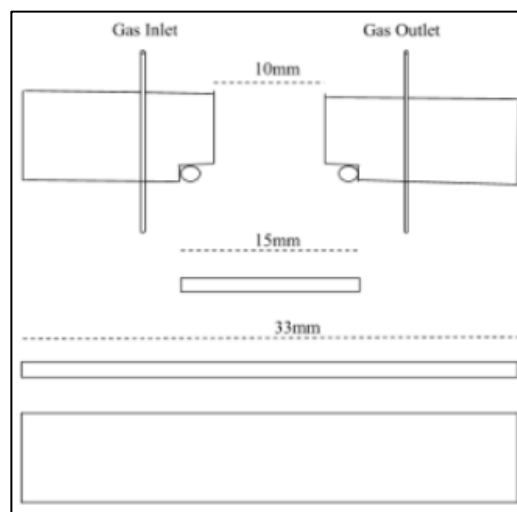


Figure 6: 2-D design schematic for reactor chuck alterations needed to facilitate the inclusion of pyrometer.

To facilitate accurate measurements by the pyrometer, while maintaining a pressurized reaction chamber with minimized dead space, it was important to closely consider the material used for the window. Foremost, it was necessary to consider materials that are reasonably optically transmissive in the wavelengths that the pyrometer detects. The Optris CTlaser 4M pyrometer employed in our design has a spectral range of 2.2 to 6 μm .²¹ Some materials commonly used for infrared (IR) applications include potassium bromide, sodium chloride, magnesium fluoride, calcium fluoride, sapphire, zinc sulfide, zinc selenide, fused silica, N-BK7, silicon, and germanium.

After eliminating many of these materials based on their transmission spectra as well as stability regarding the chemical and thermal environments to which the window would be exposed, three materials of interest remained: zinc sulfide (ZnS), zinc selenide (ZnSe), and sapphire. These materials were then compared based on further specifications for each corresponding product at Edmund Optics (Table 1).²²

Geometry for each material was selected based on the desired design specifications of the reactor. The Knoop hardness, as shown in Table 1, is a measure of a material's resistance to being scratched or dented. Both ZnS and ZnSe are optically transparent in the desired range of 2.2 – 6 μm . Sapphire preforms very well in this range but is only optically transparent up to 5.5 μm . However, because of its significantly higher hardness and lower unit cost, the 12.50 x 12.50 mm Sapphire Window was selected for initial testing of the microreactor.

2.2.3 Third Iteration: Cooling Considerations

A key design challenge for attaining ms pulsed thermal catalysis is ensuring the reactor is capable of achieving a sufficiently rapid cooling rate. Therefore, external cooling is required to enhance cooling rates and as a heat-sink to limit thermal accumulation. A microchannel cooling block was selected and obtained from Micro Cooling Concepts, Inc. based on its appropriate geometry and high

cooling capacity. The selected cooler package was the SA-2A option, a water-cooled gold-plated copper heatsink with a 2 cm by 1 cm cooling surface.⁶ Enabled by internal micro-impingement cooling circuits, the heatsink can achieve thermal resistances as low as 25 K-cm²/kW with cooling water. Additionally, a manifold was purchased as a mount for the cooler and to aid in regulation of coolant inlets and outlets.

The cooling block was incorporated into the reactor design by machining a rectangular hole into the base of the reactor. The bottom piece of the reactor chuck was then shaved down so that when the cooling block is in the reactor, the cooling surface is flush with the bottom of the reactor chip, directly below the heated platinum.

2.2.4 Substrate Material Selection

The designs of the microreactor in this experiment use a substrate to support the platinum catalyst. The substrate material was selected based upon two main criteria: electrical resistivity and thermal conductivity. Because the target operating temperature for this reactor is both high and transient, the substrate material needed to be thermally conductive. Based on this requirement, the team compared common substrate materials using data obtained from companies that manufacture and source substrates. The results of this comparison are presented in Table 2 below.

Table 1: Comparison of relevant properties for proposed window materials. Includes dimensions, wavelength range, Knoop hardness, and cost.

Material [stock number]	Dimensions (mm)	Thickness (mm)	Wavelength Range (μm)	Knoop Hardness (kg/mm ²)	Unit Price
ZnS [#66-200]	12.50 \pm 0.1 diameter	2.00 \pm 0.1	0.4 – 12	210	\$165.00
ZnSe [#68-491]	12.50 \pm 0.1 diameter	2.00 \pm 0.1	0.6 – 18	120	\$165.00
Sapphire [#39-228]	12.50 x 12.50 \pm 0.1	1.00 \pm 0.05	0.33 – 5.5	1900	\$37.50

Table 2: Comparison of common substrates based on thermal conductivity.

Material	Thermal Conductivity (W/mK)
Silicon ²³	149
Silicon Oxide ²⁴	1.4
99.6% Alumina ²⁵	28
Fused Quartz ²⁶	1.4
Aluminum Nitride ²⁷	170
Silicon Carbide ²⁸	120

From these results, the team identified silicon (Si), aluminum nitride (AlN), and silicon carbide (SiC) as possible options for the substrate. These three options were then compared using electrical resistivity as the criteria. It is necessary that the substrate be sufficiently electrically insulating since the platinum strip is heated by applying a voltage to the catalyst strip. Table 3 shows the results of the comparison of electrical resistivity for the narrowed list of potential substrate materials.

Table 3: Comparison of narrowed list of substrate options based on electrical resistivity.

Material	Electrical Resistivity (Ωcm)
Silicon Oxide ²⁹	10^{14} - 10^{16}
Aluminum Nitride ³⁰	$>10^{14}$
Silicon Carbide ²⁸	10^2 - 10^6

Based on these findings, the team determined that silicon is not sufficiently electrically resistive but oxidizing a thin layer on the surface greatly enhances its electrical resistivity without significantly reducing the thermal conductivity. This makes silicon with an oxide coating a viable substrate option.

Although this material was used in some existing studies, the team also determined that aluminum nitride falls within reasonable ranges for both thermal conductivity and electrical resistivity. This, combined with the low cost of AlN and the fact that the team would not have oxidized the substrate and ensure even and full coating throughout experimentation, led the team to select aluminum nitride as the substrate material.

3.0 Methodology

3.1 Computational Heat Transfer Model

The purpose of this reactor is to test the application of dynamic catalysis for ammonia synthesis. It is hypothesized that by oscillating the catalytic surface temperature, kinetic pathways within a catalytic cycle may be able to proceed under multiple thermodynamic conditions. Therefore, dynamic temperature control must be maintained at timescales near that of a single catalytic cycle (estimated to be around 10 – 100 ms). To determine if this was attainable based on the current specifications of the reactor, several heat transfer models regarding the reactor system were designed and evaluated using COMSOL Multiphysics V5.6 (licensing courtesy of Worcester Polytechnic Institute). In terms of the desired timescale, the first objective was to find the maximum time it would take for the platinum at the high temperature condition (200 °C) to cool to the low temperature condition (100 °C).

To simulate cooling of the platinum catalyst on the AlN wafer, several assumptions were made so that the results would articulate a maximum time scenario: the platinum is insulated at the top boundary, the wafer has had sufficient time to build up a linear gradient between the 200 °C platinum and the 20 °C

cooled surface, and only one-dimensional heat transfer in the direction of the platinum down through the AlN to the coolant is considered (no dispersion of heat in other directions). Additional assumptions include perfect thermal contact at the platinum-AlN interface and a constant 20 °C boundary condition at the AlN-aluminum interface.

Next, it was necessary to obtain initial estimates of the power inputs required to maintain the platinum at 100 and 200 °C as well as to heat it to 200 °C from 100 °C. The power to heat the platinum (P) can be calculated with equation 10, by adding the power required to generate the amount of heat that would raise the temperature of the platinum multiplied by the temperature change per unit time, dT/dt to the power lost due to cooling the reactor, $P_{cooling}$. Other variables indicate known quantities where d is density of platinum, C_p is heat capacity of platinum, l is length of the platinum strip, w is its width, and h is its height.

$$P = d \cdot C_p \cdot l \cdot w \cdot h \cdot \frac{dT}{dt} + P_{cooling} \quad (10)$$

$P_{cooling}$ was calculated in COMSOL for each of the three conditions by performing a point integration at the platinum-AlN interface to find the flux of heat out of the platinum. For the heating and maintaining 200 °C conditions, $P_{cooling}$ was found by solving the same model as before but in steady state with the platinum at a constant temperature of 200 °C. For maintaining the 100 °C condition, $P_{cooling}$ was found by solving the model with the platinum at 100 °C in steady state to obtain the point integration. Because the constant temperature conditions do not require heating, only $P_{cooling}$ is required to find the necessary amount of power to apply.

The method by which power is applied to heat the platinum is by conducting current (I)

through it, resulting in a voltage drop (V) across the platinum. Based on equation 11, the platinum with resistivity ρ , length l , and cross-sectional area $w \cdot h$ will have a resistance of R. Finally, by solving equations 12 and 13 for I and V respectively, the required current and voltage can be evaluated for each temperature condition.

$$R = \frac{\rho \cdot l}{w \cdot h} \quad (11)$$

$$P = I^2 R \quad (12)$$

$$P = I \cdot V \quad (13)$$

3.2 Proof of Theory

Prior to purchasing AlN substrates, fabricating the final reactor chips, and testing the reactor, the team set out to accomplish three main objectives: 1) to prove that the pyrometer proposed for this project can accurately gauge temperature and simultaneously determine the relationship between the output voltage and the temperature it, 2) to prove that resistive heating can be used to heat a thin strip of platinum deposited on a substrate, and 3) to integrate the pyrometer into a temperature control loop. In this section of methodology, the steps taken to achieve these goals are discussed.

3.2.1 Pyrometer Performance/Calibration

In order to determine if the pyrometer could accurately gauge temperature, the team compared temperature readings obtained by the pyrometer to those of a thermocouple. First, a small steel slide was obtained and placed on a hotplate in the off position. Next, a thermocouple was obtained, and the probe of the thermocouple was placed in contact with the steel. The pyrometer was then mounted

above the steel piece such that the focal point was at the surface of the plate, per the pyrometer specifications. Additionally, the leads of a multimeter were connected to the output voltage pins on the pyrometer such that the output voltage corresponding to each temperature could be recorded. Figure 7 below depicts the experimental setup used during this testing.

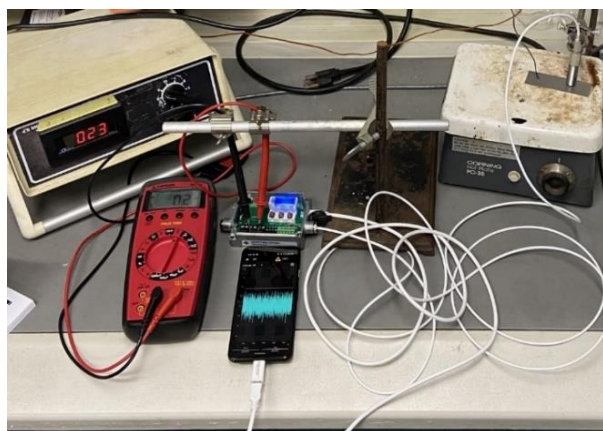


Figure 7: *Experimental setup for pyrometer calibration. Includes thermocouple, multimeter with leads in pyrometer output pins, hotplate, steel slate.*

The team then proceeded to increase the temperature of the steel piece using the hotplate, and recorded the temperature from the pyrometer, the temperature from the thermocouple, and the voltage output from the pyrometer. These were then plotted to determine the accuracy of the pyrometer as well as the relationship between output voltage and temperature.

3.2.2 Proof of Heating

The first step in determining if heating could successfully be achieved across a chip with a platinum strip on a supporting was fabricating the chip. Based on accessibility, cost, and the ability to dice and treat in house, silicon was selected for this process. In order

to properly prepare the silicon, the material was first diced to the appropriate dimensions. This was done using a steel wheel glass cutter lubricated with oil to score the wafer. The wafers were then snapped along a counter edge and any roughness on the along the break was buffed out using sandpaper. Following dicing, the substrates were cleaned using a supersonic bath to remove oils and surface contaminants. This process was achieved by placing the wafers into a beaker and adding isopropyl alcohol until they were fully submerged. Water of approximately one inch depth was filled in a supersonic bath. The beaker was then placed in the basin and the bath was run for five minutes. This process was repeated using acetone, then the wafers were removed, rinsed with deionized water, and placed in a furnace at 100 °C.³¹

Once the wafers were fully dry, the resistance was taken across the surface. For testing the resistance in this step and all subsequent resistance tests unless otherwise stated, the resistance was taken by placing copper foil between the substrate and a glass microscope slide at a specified and consistent distance. A binder clip was then applied to sandwich the substrate and glass microscope slide together with a relatively even and repeatable pressure. The alligator clips of a multimeter were then attached to the copper foil strips and the resistance was recorded. This process removed some of the variability associated with measuring resistance including uneven pressure and distance between multimeter leads from sample to sample.

For the purpose of this application, the substrate is required to be electrically insulating to ensure that the path of least-resistance is through the platinum catalyst strip. For this reason, the silicon substrates were oxidized in a tube furnace. For all chips, air flow was supplied across the substrate surface

while in the tube furnace. Following oxidation, the resistance was again measured across the surface of the substrates to ensure that the oxide layer formed was sufficiently electrically insulating.

After oxidation, the silicon substrates were sputtered with the platinum and gold contacts as proposed in the initial design considerations. This was achieved by first masking the substrates with masking tape such that only the desired width of the platinum catalyst surface was exposed as a strip down the middle of the substrate. The pieces were then sputtered under conditions informed by the team's experienced sputterer operator.

Once the platinum was successfully deposited, the masking tape was removed, acetone was used to remove any tape residue, and each chip was again masked for application of the gold contacts. This was done by placing a piece of paper in the middle of each strip then applying masking tape to cover the platinum strip in a band-aid-like way. This ensured that the platinum strip was not damaged while removing the masking tape after sputtering. The resistance across the platinum strip was then measured, concluding the fabrication of the SiO_2 substrates.

Once the substrates were fabricated, the team began testing the heating functionality of the chip. First, the chip was mounted in the reactor chuck. Leads were then created by placing copper foil on top of the gold contacts on each end, placing a small piece of glass on top of the copper, then sandwiching the layers together using a clip. This configuration was then tested for shorts to ensure that electricity was not being conducted between the chip and the reactor. The chip was then connected to the power supply by placing the power supply leads onto the ends of both copper strips then placing the sense leads on the copper strips between the power supply

leads and the chips. Finally, the pyrometer was mounted on the reactor. The experimental setup for this testing is given in the image below.



Figure 8: *Experimental setup for proof of theory heat tests. Includes reactor, power supply lead, and sense lead configuration.*

With this experimental set up, the team then conducted a series of tests wherein a voltage was applied, and the change in temperature was recorded.

3.2.3 Temperature Control Loop

In order to integrate the pyrometer into a temperature control loop, the team first tested a small piece of steel shim. The piece was approximately 0.007" and was directly connected to the leads of the power supply with alligator clips. The sense leads were not placed on the steel, but rather connected to the output pins of the pyrometer. The pyrometer was situated above the steel at 50 mm to achieve the setup depicted in Figure 9.



Figure 9: Experimental setup for temperature control tests. Includes steel strip connected to power supply with pyrometer and sense leads connected to pyrometer output.

The team was then able to use this experimental setup in conjunction with the relationship between voltage output and temperature as determined through per section 3.1.1 above to control temperature. This was achieved by entering the output voltage that corresponds to a certain temperature into the power supply. When activated, the power supply applied voltage to get to and maintain the desired temperature. In this sense, by connecting the sense leads to the pyrometer output, a control loop was established. A series of tests were run by increasing the temperature setpoint by altering the corresponding voltage input into the power supply and recording the resulting temperature versus time profile. From these data, the time to heat was observed as well as the overshoot and time to stabilize at different temperatures. Additionally, the team conducted tests altering the current limit for the same temperature to determine the effects of current limit on time to heat and overshoot.

3.3 Final Reactor Fabrication and Testing

3.3.1 Experimental Design

The proposed reactor design for experimental analysis of thermally pulsed

catalysis is given in Figure 10. Certain experimental setups excluded or altered components of this design, such as gas flow with the mass spectrometer (MS), location of the power supply sense leads, or flow of the cooling water (CW).

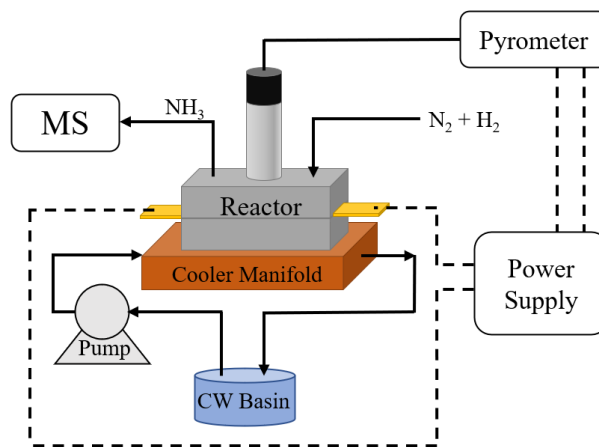


Figure 10: Final reactor design schematic with N_2 and H_2 feed and NH_3 product stream to a mass spectrometer (MS) for analysis. Here, the sense leads of the power supply are connected to the voltage output of the pyrometer for direct temperature control.

3.3.2 AlN Chip Fabrication

Prior to producing the AlN chips, access to the sputterer used to produce the SiO_2 chips was lost. As a result, the team needed to determine an alternative method of depositing a thin film of platinum on an AlN substrate. After literature review, a modified sol-gel processing technique that has proved effective for glass surfaces was attempted.³² The treatment solution was prepared by combining hexachloroplatinic acid (H_2PtCl_6), citric acid, and ethylene glycol at a molar ratio of 1:8:32, respectively. First, 0.859 g of citric acid was dissolved in 1 mL of ethylene glycol at 60 °C for approximately 1 hour. Next, 0.229 g of H_2PtCl_6 was added to the solution and allowed to fully dissolve over the course of 12 hours.

This resulted in a slightly cloudy, viscous solution.

Initially, the team attempted a masking and coating procedure by placing tin foil over the regions that were not going to be coated, leaving a 4 mm wide strip exposed down the middle of the AlN chip. The slurry was then painted over the exposed strip with a cotton swab and the chip was placed in a tube furnace for thermal treatment, which was required to facilitate formation of the platinum film. In a tube furnace, the AlN chip was treated at 130 °C for 30 minutes to dehydrate the solution, then at 250 °C for 30 minutes to improve adherence of the film, and finished at 500 °C to remove any remaining organic compounds from the solution. This thermal treatment process was repeated several additional times, each following the reapplication of the platinum solution. In total, the coating and heat-treating process was repeated between 4 and 6 times before the tin foil masking was removed.

Based on the results of this process, which will be further discussed in the results section, the team made several alterations to this process. In the modified process, the team masked the substrates using Scotch tape and roughened the exposed strip using sandpaper. The slurry was then painted on the roughened strip, the masking was removed, and the substrate was heat-treated in the same thermal cycle previously described. The masking, coating, and heat-treating steps of this process were repeated and the resistance was tested following each applied layer until a desired resistance approximated between 4-14 Ω was achieved.

3.3.3 Reactor Heating Tests

In order to understand the limitations of the reactor, it was necessary to record the

temperature response profile for various applied voltages. In order to achieve this, the reactor was configured in a voltage-controlled experimental setup wherein the power supply leads and the sense leads were both connected to the copper leads of the reactor. It is important to note that since the team did not have access to a sputterer, there were no gold contacts on the reactor chip as called for in initial design considerations. Accordingly, the copper leads extended underneath the reactor gasket and the pressure applied when the reactor was compressed ensured good electrical contact between the platinum strip and the copper leads. In Figure 11, this experimental setup is demonstrated.

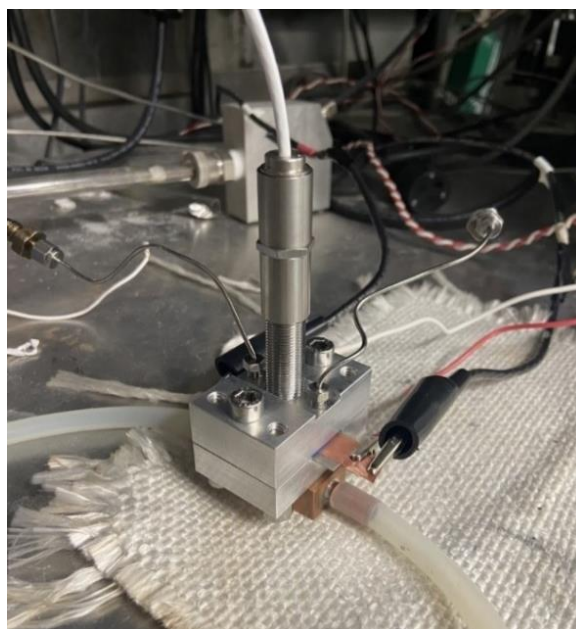


Figure 11: *Experimental setup for heating tests. Includes sense leads attached to the copper leads of the reactor, as opposed to the pyrometer output pins as in the temperature-controlled setup.*

A series of tests were then conducted wherein the power supply was programmed to supply a set voltage for five seconds, then allow ten seconds for cooling. This was repeated for voltages of 5 V, 10 V, 20 V, 30 V,

40 V and 50 V and the temperature versus time data for each voltage were recorded. This process was initially conducted with no cooling, then repeated for 3 different coolant flowrates.

3.3.4 Reactor Cooling Tests

In order for this reactor to be used in pulsed catalysis, it is also important to understand the cooling rates of the platinum surface and reactor. Accordingly, the team conducted a series of tests to determine the cooling rates from different temperatures with different coolant flowrates. This testing was conducted in the temperature-configuration of the reactor, wherein the sense leads were connected to the voltage output pins of the pyrometer. This experimental setup is depicted in the Figure 12 below.

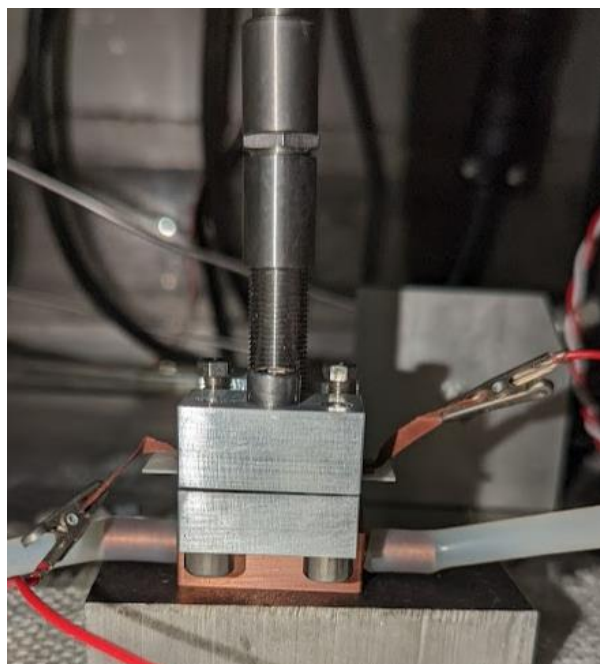


Figure 12: *Experimental setup for cooling tests. Includes reactor chuck situated on top of cooling block, pyrometer, and power supply connected to the reactor's leads.*

To maximize uniformity between tests for different coolant flowrates, the team used the programming option of the power supply to bring the platinum strip to a predetermined temperature where it was maintained for 2 seconds before the voltage was removed for 10 seconds to allow sufficient time for cooling. In a single run, the reactor was controlled to 100 °C, 150 °C, 200 °C, 250 °C, and 300 °C in the 2 seconds-on 10 seconds-off pattern described. This was conducted with no cooling, then repeated with the flowrates of 10 mL/min, 20 mL/min and 30 mL/min. For each run, the resulting temperature profile was recorded as a function of time. In addition, visual and physical observations were made during and after each run.

4.3.5 Temperature-Controlled Square Wave Tests

After characterizing the heating and cooling capacities of the reactor, the next step in gauging the performance of this reactor was determining its square wave functionality. In order to do this, the reactor was once again configured in the temperature control setup (See Figure 12). The cooling flowrate was set to 20 mL/min where it was maintained for all tests. The power supply was programmed to complete three oscillations between two predetermined temperatures by inputting the voltage that corresponds to each temperature. The program was configured such that the temperature remained in the high and low temperature regimes for a given dwell time before switching. Table 4 provides the temperatures of the high and low temperature regimes. Additionally, the dwell times for all trials that were run during this testing are recorded. For each trial, the temperature versus time data were recorded using the pyrometer software interface.

Table 4: Predetermined temperatures and dwell times for temperature-controlled square wave tests. The Low-High designation corresponds to the low setpoint and high setpoint between which the oscillations occur with dwell time corresponding to the amount of time in each regime.

Trial Number	Temperature (°C)	Dwell Time (s)
	Low-High	
1	100-150	5
2	100-200	5
3	100-250	5
4	100-300	5
5	100-150	2
6	100-200	2
7	100-250	2
8	100-300	2
9	100-150	1
10	100-200	1
11	100-250	1
12	100-300	1
13	100-150	0.5
14	100-200	0.5
15	100-250	0.5
16	100-300	0.5

4.3.6 Reactor Sealing Tests

The end goal of this reactor is to be used for reaction chemistry. Accordingly, the reactor chamber must be airtight. In order to determine where alterations must be made to ensure proper sealing, the reactor was subjected to a simple bubble test. First, the reactor was integrated into an existing flow system equipped with multiple gas tanks, pressure gauges, and a downstream flowmeter. The experimental setup for this test is shown in Figure 13 below.

Gas flow was initiated through the reactor. By applying a mixture of soap and water, each junction was tested for leaks starting from the gas inlet flow on the far left and working through each connection in the reactor to the gas outlet flow on the far right. If the production of bubbles was observed at a point in the reactor, the local bolts and connectors were tightened and the location was retested. If this did not resolve the leak, the leak was noted and temporarily sealed using Teflon tape. Each time a leak was identified and addressed, the team restarted the test from the gas inlet, to ensure that alterations downstream did not induce a leak at a previously tested location.

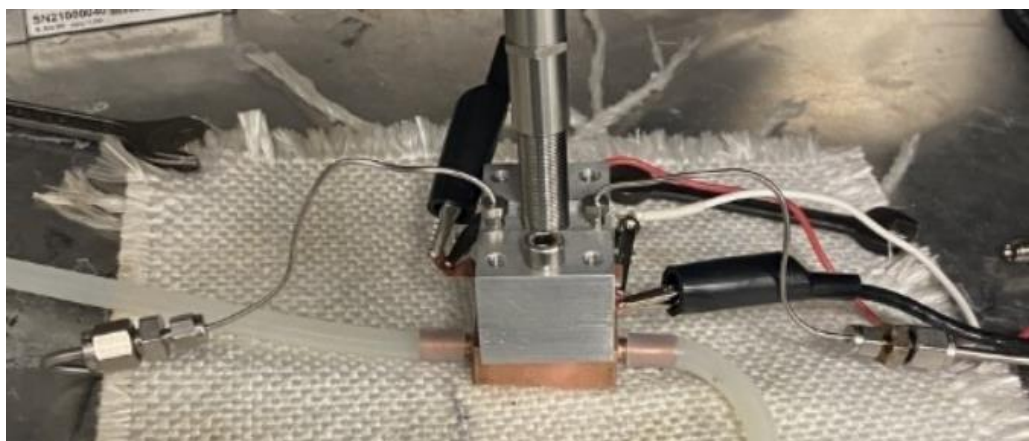


Figure 13: Experimental setup for seal testing. Key setup is gas flow tubes emerging from top of reactor and connecting to existing flow system. Gas inlet is on the left and outlet is on the right-hand side of the reactor respectively.

4.0 Results and Discussion

5.1 Reactor Fabrication

With the considerations outlined in section 2.2 of this paper, the team was able to successfully fabricate a microreactor suitable for pulsed catalysis. The resulting reactor chuck is given in the Figure 14 below.



Figure 14: Final fabricated reactor chuck

5.2 Computational Heat Transfer Modeling

Based on COMSOL heat transfer analyses, several estimations were made regarding the power to heat and time to cool for the reactor chip, as shown in Table 5 and Figure 15. After simulations were completed, COMSOL suggested it would take approximately 0.8 ms for the platinum catalyst to cool down 100 degrees from in initial temperature of 200 °C, well under what would be required to operate within the timescale of a catalytic cycle. With a chosen heating time of 0.1 ms and maintaining each constant temperature condition for a time interval of 10 ms, the estimated heating requirements for

each of these conditions were found, as shown in Table 5.

Table 5: Heating requirements for thermally pulsed temperature regimes based on COMSOL results.

Starting Temp. (°C)	Time Interval (ms)	Final Temp. (°C)	Power (J/s)	Voltage (V)
200	Δt_c	T1	0	0
100	Δt_{T1}	100	9.92	16.2
100	Δt_h	200	32.1	29.2
200	Δt_{T2}	200	27.6	27.0

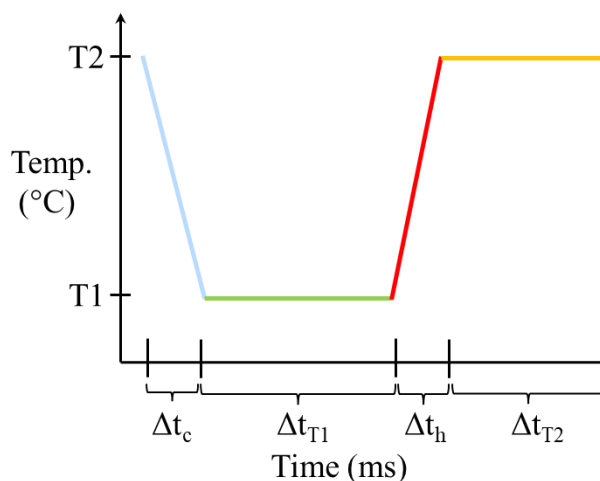


Figure 15: Ideal temperature versus time profile as informed by the power requirements determined through COMSOL

This simulation validates the theoretical basis for this design by suggesting that a thin platinum catalyst is capable of being resistively heated and conductively cooled on time scales faster than those required for pulsed catalysis. Based on these calculations, the team proceeded with experimentally confirming the viability of this reactor design.

5.3 Proof of Theory

5.3.1 Pyrometer Performance/Calibration

The accuracy of the pyrometer and the relationship between temperature and voltage output was determined by collecting the temperature measured by the pyrometer, the temperature measured by a thermocouple, and the voltage output of the pyrometer for a piece of steel heated on a hot plate. The temperature of measured by the pyrometer and the temperature measured by the thermocouple were then plotted as a function of the output voltage to obtain the Figure 16.

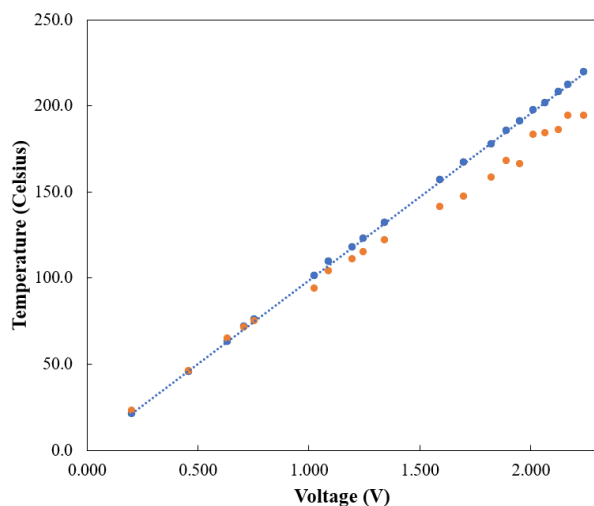


Figure 16: Plot of temperature measured by pyrometer (blue) and temperature measured by thermocouple (orange) as a function of the output voltage of the pyrometer. Figure includes best fit line for output voltage versus temperature measured by pyrometer.

As shown in figure 16, there is a strong linear 100:1 correlation between the pyrometer temperature reading in degrees Celsius and the voltage output recorded according to the setup detailed in the methods section. The thermocouple strongly corroborates the accuracy of the pyrometer temperature measurements up to around 100 °C. After this

point, the deviation between the temperature measured by the pyrometer and the temperature measured by the thermocouple becomes increasing significant. It is hypothesized that the divergence between pyrometer and thermocouple measurements after this point is likely due to poor thermal contact between the thermocouple and heated plate leading to a significant latency in accurate measurements as temperatures increases.

The precision of pyrometer measurements at various temperatures were determined based on the results of controlled temperature oscillation experiments detailed later in this report (Table 6).

Table 6: Precision of pyrometer at different operating temperatures as indicated by the error associated with temperature readings. As shown, as temperature increases, the pyrometer becomes more precise.

Temperature (°C)	Error (°C)
22	± 7.3
50	± 1.9
100	± 0.4
150	± 0.15
200	± 0.05
250	± 0.05
300	± 0.05

Based on these error measurements, the pyrometer is clearly better suited for measurements at temperatures above 100 °C. At or above 200 °C, the pyrometer remains accurate within a margin of 0.1 °C. Higher precision at elevated temperatures is because of better signal to noise ratios due to more infrared output.

5.3.2 Proof of Heating

Via the fabrication method outlined in the methodology chapter of this paper, platinum catalyst strips and gold contacts were successfully deposited on Si/SiO₂ supporting substrates. An example of the resulting chip is shown below.

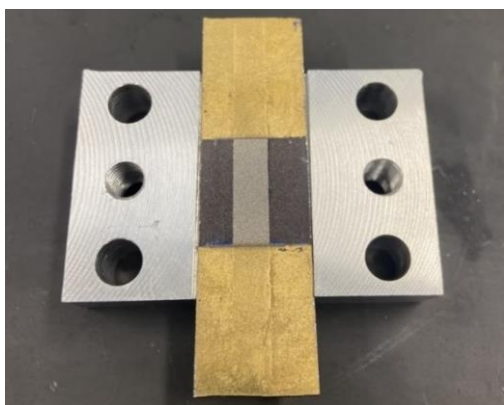


Figure 17: Photograph of fabricated SiO₂ chip situated in reactor base.

By applying a voltage, the team successfully leveraged resistive heating to increase the temperature of a platinum strip sputtered on a supporting SiO₂ substrate. While the resistive heating was successful in the low range of temperatures, the chip did not display the same functionality at elevated temperatures. Instead, each chip lost

functionality as testing demanded higher temperatures. The team came to believe that this loss of functionality, which was characterized in the temperature versus time profiles by a sharp decrease in temperature, was not occurring when the chip reached elevated temperatures, but rather at a critical voltage that fell between 10-20 V for each chip. At that voltage, the chip sustained significant and irreversible damage resulting in a significant decrease in resistivity. This indicated that the current was finding a path of lesser resistance, which the team attributed to the nature of Si. The findings of this section corroborated the theory that resistive heating could be used to heat a platinum catalyst strip and further motivated the team's decision to use AlN as the substrate material as opposed to SiO₂.

5.3.3 Temperature Control Loop

By connecting the sense leads to the pyrometer output, the team was able to successfully integrate the pyrometer into a temperature control loop. This can clearly be seen in Figure 18, wherein the temperature was increased stepwise in 20 °C intervals from room temperature to 200 °C. As shown, the

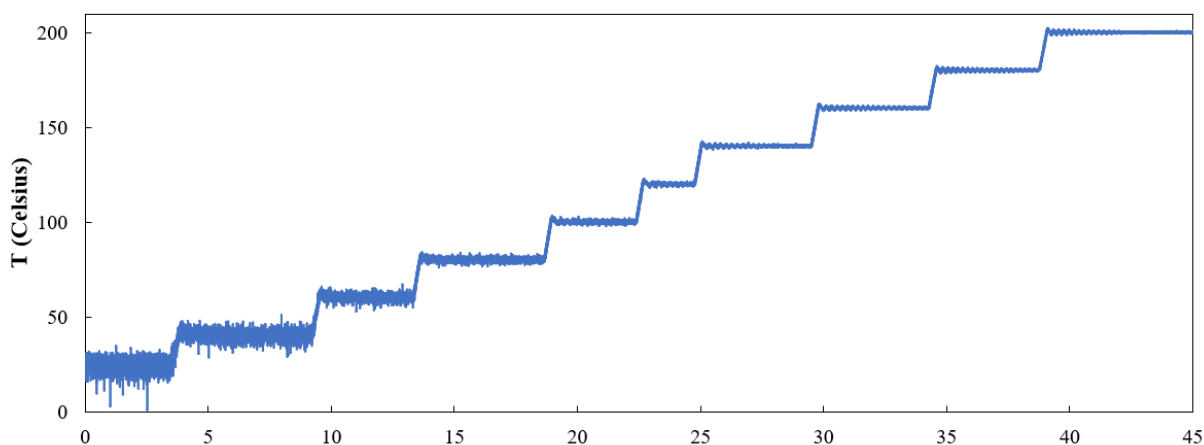


Figure 18: Temperature versus time profile obtained for controlled stepping from room temperature to 200 °C in 20 °C intervals.

control loop produced a temperature versus time profile similar to a P&ID controller wherein the temperature setpoint was overshoot, then oscillated about the setpoint. It was also determined that the current limit had an effect on the temperature control. The team hypothesized that this was due to the fact that the power supply applied the largest possible voltage for the given current limit. Based on this, manipulating the current limit altered the voltage applied during the heating portion of the graph, which had significant implications for the time of heating, the overshoot above the temperature setpoint, and the time until the temperature stabilized at the setpoint. This can be seen in Figure 19, which compares the heating profiles obtained when using the temperature control loop to heat the steel strip from room temperature to 75 °C for a current limit of 10 A, a current limit of 15 A, and a

current limit of 20 A. As depicted in the figure, when operating the reactor in the temperature control loop, the current limit determines the rate of heating and the overshoot. As the current limit increases, the heating rate also increases. This can be seen in comparing the heating time of the 20 A current limit versus 10 A current limit trials as given in Figure 18, which took approximately 0.17 s and 1 s respectively. Also, as the current limit increases the magnitude of the overshoot also increases, as shown through the 15 °C, 10 °C, and 5 °C magnitude overshoot for the 20 A, 15 A, and 10 A tests respectively. It is important to understand that much of the overshoot is likely due to the feedback delay in the loop because the pyrometer must gauge the temperature and generate an output voltage, that is then returned to the power supply.

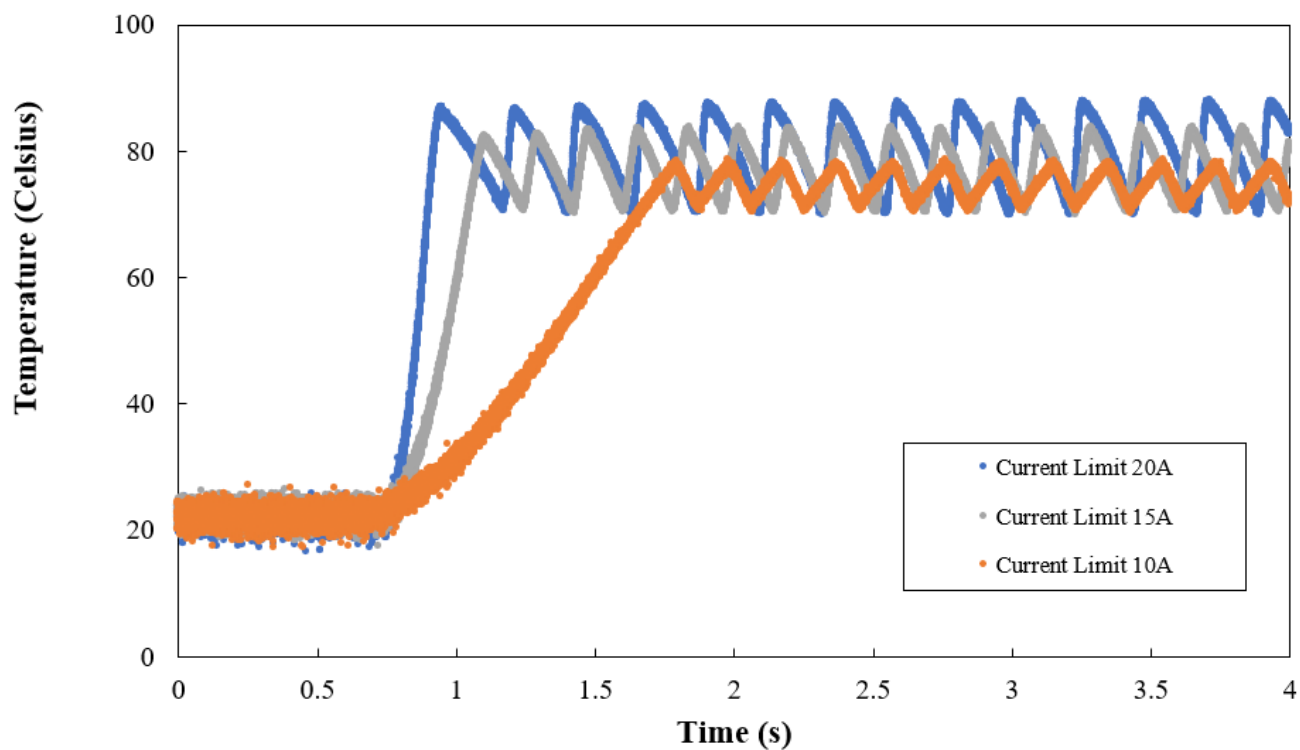


Figure 19: Temperature versus time profile obtained for controlled heating from room temperature to 75 °C with different current limits.

5.4 Final Reactor Fabrication and Tests

5.4.1 AlN Chip Fabrication

Using the modified sol-gel processes described in the methodology section of this paper, the team was able to deposit Pt catalyst strips on AlN substrates. In initial attempts at this process, the team cleaned the substrates and applied the slurry without additional surface treatment. The main disadvantage that the team observed was poor surface interactions with between the substrate and the viscous liquid. Specifically, the slurry had a tendency to bead up and adopt a relatively large contact angle, which created resulting platinum strip with variable width. This also resulted in variable thickness across the platinum strip. An additional issue with this method arose from the masking technique, which used tin foil. Because the tin foil was not fully flush against the surface, a capillary action-like effect was observed wherein the slurry was pulled under the foil and around the edges of the material, resulting in platinum deposition outside of the desired locations.

In order to address these issues, the team started with a qualitative test regarding the contact angle formed between the substrate and the slurry. In the case of water, many hydrophobic materials adopt a greater contact angle as roughness increases and many hydrophilic materials adopt a lesser contact angle as roughness increases. Inspired by this principle, the team set out to determine if slurry-substrate pair displayed roughness-induced behavior that could be leveraged to produce a more uniform platinum film. To test this, the team took an AlN substrate and roughened half of it using sandpaper. The substrate was then cleaned to remove any residue from sanding and dabbed different volumes and shapes of the slurry on both the

sanded and untreated halves of the substrate to compare.

The team immediately noticed that the slurry on placed on the untreated surface beaded up, while the slurry placed on the roughened surface produced a much lower contact angle, resulting in coatings with more uniform thickness. Additionally, the team observed that, over the course of a few minutes, the slurry continued to bead up, pooling in from the outer edges of droplets. Conversely, the team found that the slurry dabbed on the roughened portion of the substrate retained its dimensions over the same timeframe.

Based on these findings the team determined that roughening the substrate surface allowed the slurry to be applied more evenly and resulted in preferential interaction with the roughened portions. The later finding eliminated the need for masking beyond initial painting and thus the process was modified. The revised the coating process called for masking with Scotch tape, roughening the strip that was to be coated, and painting the slurry on before removing the tape and heat treating as before. Reactor chips fabricated via the two different coating methods are compared in Figure 19.

Even under this improved processing technique; however, the platinum resulting strips had several limitations. Firstly, the resulting platinum film was highly porous. This is not ideal for this application since porosity makes for a torturous path for current. Additionally, the process resulted in improvements relative to previous attempts, but overall, the film was still considered non-uniform. This was confirmed through resistance testing which revealed variability in the resistance measure across different portions of the chip.

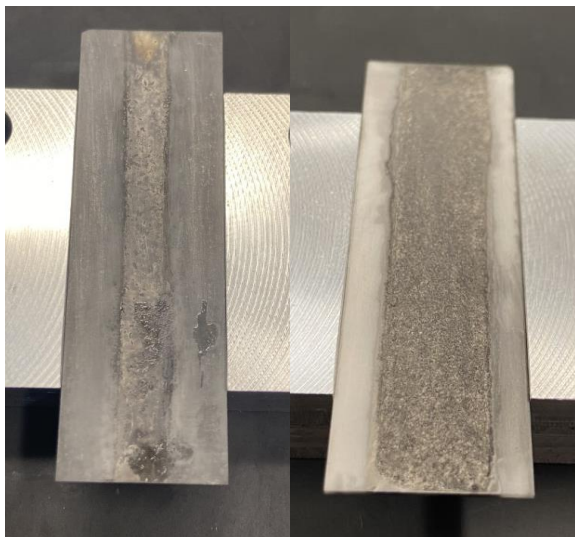


Figure 20: Reactor chip fabricated via initial process (left) and modified process (right).

Finally, another major disadvantage of this process was that it was extremely difficult to replicate chips. This meant that each chip had slightly different set of properties, making it difficult to compare the results of heating and cooling tests across chips. Accordingly, the team utilized the same reactor chip for all of the tests going forward.

5.4.2 Voltage Heating Tests

The voltage requirements to induce and maintain elevated temperatures were tested on the AlN-platinum reactor system for various cooling conditions. This was performed by applying 10, 20, 30, and 40 volts across the catalyst for a period of 5 seconds each. These tests were repeated without cooling, with low coolant flow (10 mL/min), medium coolant flow (20 mL/min), and high coolant flow (30 mL/min) (Figure 20). Although none of the 10 V experiments achieved a substantial temperature change, the higher voltage experiments show rapid heating to operationally relevant temperatures (See Appendix B). After 5 seconds at 40 V, for coolant flows of 0, 10, 20, and 30 mL/min, the catalyst reaches 204, 194, 188, and 186 °C, respectively. These are relatively close with respect to their associated temperature changes, where the baseline temperature is lower for higher cooling conditions. Therefore, heating rates are analyzed based on controlled heating tests for intentionally targeted temperature changes.

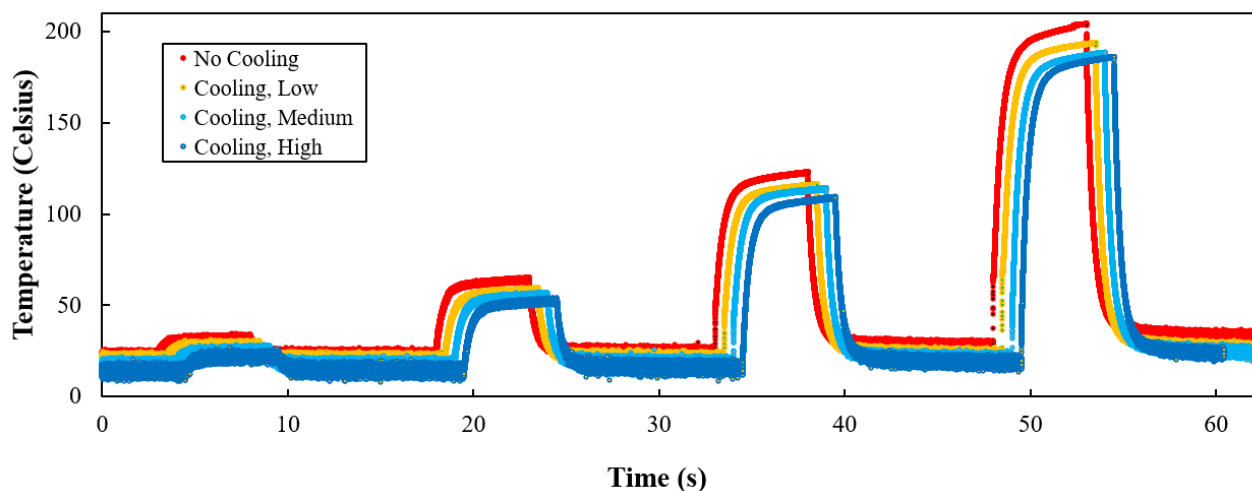


Figure 21: Temperature versus time profiles obtained from applying a given voltage for 5 seconds for trials with no coolant, 10 mL/min coolant flow, 20 mL/min coolant flow, and 30 mL/min coolant flow. In order from left to right, the peaks observed in the figure correspond to the application of 10 V, 20 V, 30 V, and 40 V respectively.

As depicted in the figure, applying 10 versus 20 V results in an increase in the stabilization temperature of between 30-33 °C. Similarly, in comparing results for 20 V to 30 V, this increase was between 57-59 °C and from 30 V to 40 V this increase was between 74-81 °C. Based on these results, oscillations within the desired temperature regimes should be achievable as maintaining temperatures between 100 °C and 300 °C for all cooling flows requires voltages within the limit of the power supply.

5.4.3 Reactor Cooling Tests

Incorporation of a cooling block in the bottom of the reactor, flush with the bottom of the AlN substrate, enhanced rapid cooling of the platinum catalyst and prevented thermal accumulation in the reactor chuck. Without cooling, for the most catalytically relevant temperature change, the platinum cools from 300 °C to 200 °C in 0.2537 seconds. For coolant flows of 10, 20, and 30 mL/min, this same temperature change is achieved in 0.2212, 0.2207, and 0.2255 seconds, respectively. For cooling intervals of 100 °C across all tested coolant flows, there is a 30% to 34% decrease in cooling time when comparing cooling domains of 200-100 °C to 250-150 °C. Furthermore, cooling from 300 to 200°C is 18% to 23% faster than for 250 °C to 150 °C. Decreases in cooling time at elevated temperature domains is especially promising

for pulsed catalytic experiments that require higher temperatures than those discussed here. For a complete table of these cooling time data, see Appendix C. Additionally, these cooling experiments indicate an optimized coolant flow for future use of the reactor. From no cooling, to 10 mL/min, to 20 mL/min, there is a successive decrease in cooling time across various targeted temperature changes outlined in Table 6.

For 300-200 °C, the cooling time is reduced by 0.0325 seconds with a 10 mL/min flow, and another 0.0005 seconds faster when the flow is increased to 20 mL/min. However, when the coolant flow is increased to 30 mL/min, the cooling rate increases in comparison to 10 and 20 mL/min. This increase is about 0.0048 seconds when comparing 30 to 20 mL/min for 300-200 °C. Therefore, although the change in cooling time from 10 to 20 mL/min is relatively small, the difference is consistently measurable, so the coolant flow can be optimized around 20 mL/min. At this optimized flow, a 300 °C to 200 °C change is about 15% faster than without cooling (Table 7).

In addition to the quantitative results obtained via the cooling tests under different conditions, it is also important to note that the team made several important qualitative discoveries regarding the functionality of the cooling block as well. Firstly, the team noticed that at elevated coolant flowrates, air pockets developed in the tubing due to lower pressures

Table 7: Time to cool and cooling rates for cooling from 300-200 °C, 250-100 °C, and 200-100 °C. For each 100 °C increment the resulting times and rates are recorded for no coolant flow, 10 mL/min, 20 mL/min, and 30 mL/min.

T ₁ -T ₂ (°C)	Time to Cool (s)				Cooling Rate (°C/s)			
	$\dot{v} \left(\frac{\text{mL}}{\text{min}}\right) = 0$	10	20	30	0	10	20	30
300-200	0.254	0.221	0.221	0.226	394	452	453	443
250-150	0.300	0.271	0.266	0.270	334	368	376	371
200-100	0.393	0.364	0.349	0.352	255	275	287	285

induced by the higher flow. The team hypothesizes that the attenuated cooling performance at 30 mL/min may be attributed to this phenomenon.

The team also noted that the aluminum base of the reactor chuck was cold to the touch in all trials that included coolant flow. Conversely, the reactor was hot to the touch following the tests without cooling, even these tests only subjected the reactor to intermittent heating for no more than a few minutes. This is an important observation as it demonstrates that heat accumulation can occur in the reactor chuck if the system is not properly cooled. While this had little perceivable effect on the tests conducted here, the team believes this type of heat accumulation would more significantly influence the heat transfer properties of the reactor as the time of operation increases.

Moreover, several reactor chips fractured throughout the course of this project, but this only occurred during testing without cooling. Since the temperature of the AlN was not directly monitored, the team cannot directly attribute this behavior to temperature related effects, but believe the fracturing may be instigated by heat accumulation in the substrate under no-cooling conditions.

5.4.4 Temperature-Controlled Square Wave Tests

The temperature-control system enabled rapid oscillation of temperature with a nearly-square wave profile. This allowed the team to study the reactor's performance under conditions in close resemblance to those desired for dynamically pulsed conditions. The resulting square wave temperature versus time profile for various magnitudes of temperature change is presented in Figure 22.

Based on this profile, the heating rates relevant to pulsed square wave operation of the reactor are summarized in Table 8.

Table 8: heating times and rates for temperature transitions from a starting temperature, T_1 to predetermined temperature setpoint, T_2 . These trials were conducted with 20 mL/min coolant flow.

T_1 (°C)	T_2 (°C)	Time (s)	Rate (°C/s)
100	150	0.0815	613.5
100	200	0.1846	541.7
100	250	0.2921	513.5
100	300	0.4097	488.2
200	300	0.2607	383.6

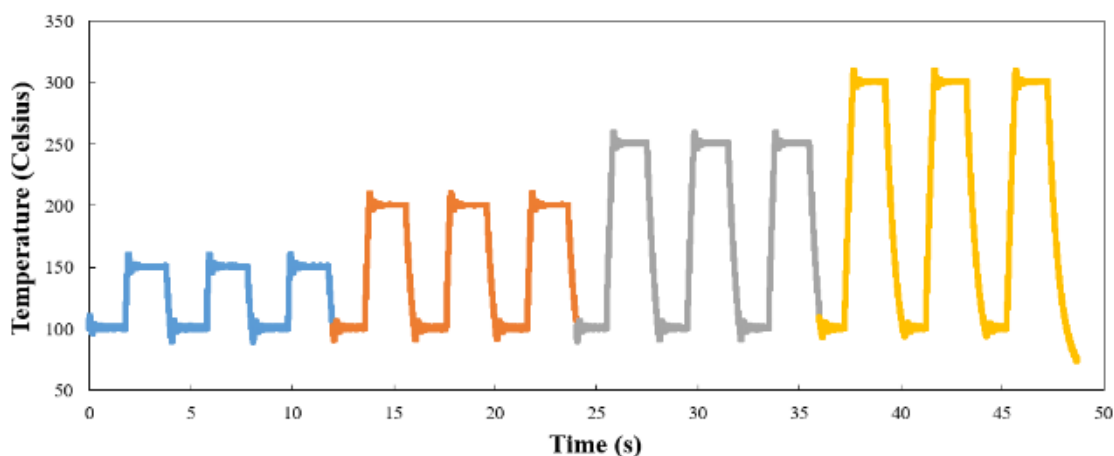


Figure 22: Square wave temperature oscillations for 100-150 °C, 100-200 °C, 100-250 °C, and 100-300 °C with a 2 s dwell time in each regime.

Heating rates for lower temperature regimes are markedly faster than for elevated temperatures: a 100 °C increase takes about when starting from 100 °C is about 144% faster than when starting from 200 °C. Heating from 100 °C to 150 °C is well within the desired heating timescale, requiring less than 82 ms to make the transition. Larger transitions at elevated temperature regimes are over 100 ms, but still only a fraction of a second.

While this timescale falls outside of the desired ranges for elevated temperatures, it is believed that alterations to the platinum catalyst such as decreasing the resistance could be enough put these heat transfer rates within a timescale appropriate for pulsed catalysis.

The heating and cooling rates for square-wave operation of the reactor remain consistent with those described above. However, maintaining temperature control for sufficiently fast square wave oscillations is dependent on the response time, or latency, of the control system. In these pulsed experiments, the system's latency manifests as an overshoot of temperature when heating. This is denoted by the difference between the peak temperature reached and the temperature setpoint.

Conversely, when cooling, undershoot is the difference between the lowest temperature reached and the target temperature. Additionally, latency in the control system influences the stabilization time, or the time it takes for the control system to maintain a reasonably isothermal state at the target temperature. Our results indicate that all of these factors are present and a major limitation to the efficacy of the current control system. Overshoots and stabilization times for various relevant temperature transitions are outlined in Table 9.

Table 9: *Overshoot magnitudes and stabilization times for controlled temperature transitions from T_1 to T_2 with 20 mL/min coolant flow.*

T1 (°C)	T2 (°C)	Overshoot (°C)	Stabilization Time (s)
50	100	11.0	0.3203
100	150	10.5	0.3048
100	200	10.2	0.1780
100	250	10.0	0.1720
100	300	9.5	0.1695
>150	100	10.0	0.3106

The stabilization time for the catalyst to reach a targeted temperature remains a significant limitation to the achievable frequency of temperature oscillations. For both heating and cooling between 100 °C and 150 °C, the time to stabilize is around 0.31s. For higher temperatures of 200 °C, 250 °C, and 300 °C, the stabilization times are 0.178, 0.172, and 0.170 seconds, respectively.

The quicker stabilization at higher temperatures is a promising result as the reactor is designed for these conditions, but the stabilization time remains well over 100ms. This means that square waves do not have time to develop for higher frequency pulses, which must be addressed in future iterations of the control system. This is clearly displayed in Figure 23, which depicts the oscillation between 100 °C and 150 °C as well as between 100 °C and 200 °C with a dwell time of 0.5 s at each temperature. In these oscillations, it is clear to see that a sharp square is not obtained.

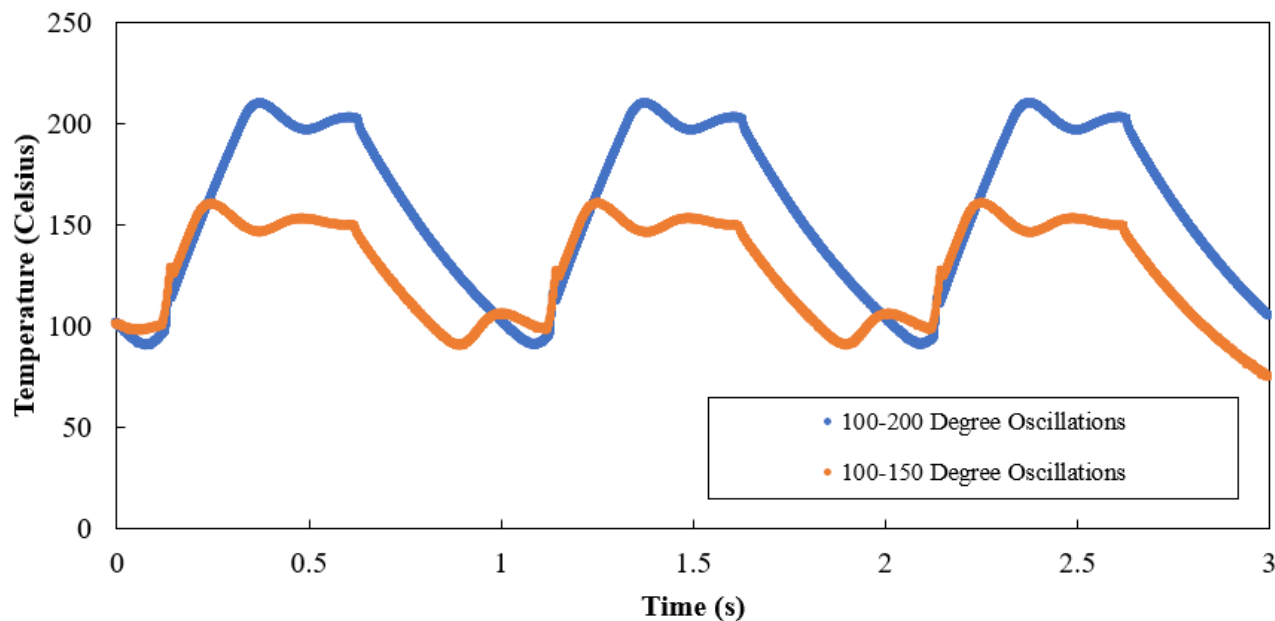


Figure 23: Temperature versus time profile obtained for oscillations between 100-150 °C and between 100-200 °C for a 0.5 s dwell time.

5.4.5 Reactor Sealing Tests

When the reactor was fully configured in the existing gas flow system and helium was supplied, the team immediately made two observations. Firstly, the downstream flowmeter was not registering any flow. Secondly, the pressure gauge at the gas inlet registered a higher increase in pressure than that experienced by the reactor that is typically used in this configuration. However, the reactor typically utilized in this gas flow system has a 1/8" inlet flow, while the team's microreactor uses a reducing fitting to accommodate a 1/16" gas inlet tube. Accordingly, the team hypothesized that the pressure increase may be due to the pressure change associated with changing diameter.

In order to test this theory, the gas inlet tube was removed from the reactor and placed into a beaker of water. The team observed air bubbles developing in the water, indicating that the tube was allowing flow. Additionally, the pressure recorded by the pressure gauge

remained constant, indicating that the higher pressure than expected was due to the change in diameter of tubing prior to entering the reactor.

Having established that a blockage was unlikely, the lack of flow as indicated by the downstream flowmeter suggested that the reactor was experiencing a significant leakage. Using a simple leak test, the team identified the first leak around the tapped hole for the pyrometer. This meant that the window was not sealed, which was expected since the current design did not allow enough space to include a gasket between the window and the lid of the reactor chuck. In order to progress with leak testing, the threading of the pyrometer was sealed using Teflon tape. With the pyrometer temporarily sealed, the team was able to identify the next leak, which was located at the copper leads of the reactor, which was also expected due to the significant difference in height between the copper and the AlN substrate.

5.0 Conclusion

Although attempts to optimize the heterogeneous catalysis of ammonia synthesis over the years have yielded a wealth of scientific discovery, the Haber-Bosch process remains markedly inefficient in conversion and highly energy-intensive in functionality. Thermally pulsed catalysis shows significant promise for lowering the energy barrier and increasing conversion for such a process, but past efforts have fallen short of proving the theoretical validity of this method. Through this project, our team has made progress towards this end by designing and fabricating a catalytic microreactor and integrating the following functionalities:

- A catalytic reaction chamber capable of rapid resistive heating;
- A mechanism for rapid cooling of the catalyst surface;
- A microsecond responsive temperature monitoring and control system.

The platinum catalytic surface was successfully deposited onto an electrically insulating AlN chip fitted to the reactor. Resistive heating to and from catalytically relevant thermodynamic regimes was achieved in under 100 ms for some transitions, and was around 260 ms from 200 °C to 300 °C. Incorporation of a micro impingement cooling block enabled rapid cooling, under 300 ms for 100 °C transitions at high temperatures. And for microsecond monitoring of the catalytic surface temperature, a high-speed pyrometer and sapphire window were included in the reactor, allowing for precise control over reaction conditions. The synergy of these distinct components facilitates a novel approach to the experimental realization of pulsed thermal catalysis for selective ammonia synthesis.

6.0 Future Recommendations

Based on the findings discussed in this paper, the team established a foundation for future work in pulsed catalysis. Nonetheless, this project has unveiled several improvements that can be made as well as several alterations that must be made before the potential of reactor is achieved. Accordingly, the team has outlined future recommendations to address the short-term, medium-term, and long-term recommendations for the future.

6.1 Short-Term Future Recommendations

6.1.1 Catalyst Deposition

Firstly, the team identified that the platinum strip deposited via the modified sol-gel process described in the methods section of this paper is non-uniform and highly porous. This impacted the reliability of the testing and made it such that the team could not compare results obtained across different chips. Accordingly, it is suggested that future work establishes a method to produce uniform and repeatable coatings on AlN substrates. As an option, the team recommends using the sputtering technique initially proposed in this paper, which would have been conducted if not for complications regarding access to sputtering services.

6.1.2 Reactor Sealing

Leak testing of the reactor revealed two main locations do not yet seal properly. The first of these locations is at the pyrometer. In initial designs, the window beneath the pyrometer was included to address the issue of sealing. This window was meant to seal via a gasket on the reactor lid side and the same gasket used in creating the reaction chamber from underneath. Accordingly, this design

utilizes the same bolting mechanism that compresses the main gasket and creates the reaction chamber to seal the window. In practice; however, the window sizing did not include enough space for a gasket between the window and the reactor lid. Based on the input of our machinist, the team recommends purchasing a larger, circular window. The larger size of the window would allow the space for a notch to be machined into the reactor lid to house an O-ring and the circular shape increases the ease of machining.

The second location that displayed serious leakage is along the copper leads. The main cause of this leakage is that the leads extend underneath the gasket, which was required to ensure that the platinum section underneath the gasket did not heat and melt the gasket during testing. In initial designs, the team proposed sputtered gold contacts that extend beneath the gasket. Based on the thickness of the proposed contacts, it is likely that this technique would allow for proper sealing.

6.1.3 Additional Short-Term Considerations

In addition to the issues and suggestions previously described, the team also found other minor challenges wherein reactor design can be improved. Firstly, the team used sputtered gold to create electrical contact with the platinum catalyst. However, this method poses the issue of connecting the contacts to the power supply since soldering or directly applying alligator clips is likely to damage the thin film. While no significant negative impacts were perceived from compressing a piece of copper foil on the edge of the gold contact to provide a location for the power supply alligator clips, the team recommends establishing a more sophisticated solution for future iterations of this reactor.

6.2 Medium-Term Recommendations

6.2.1 Heating Rate Enhancements

Throughout experimentation, the team determined that decreasing the resistivity of the platinum film decreases the voltage input needed to achieve the same heating profile. This means that a lower resistivity increases the achievable rate of heating for a given sample. The team has established two methods of achieving this decrease in resistance: increasing the thickness of the film or increasing the width of the strip. Though either method would successfully increase the achievable heating rates, additional effects must be considered. The effects of this method on cooling rates are of significant interest and are discussed below.

6.2.2 Cooling Rate Enhancements

A major limitation of the current iteration of this reactor is the cooling rate, which stands in the way of achieving oscillations on the time scale needed for pulsed catalysis. As previously discussed, during the process of determining a new method of coating the AlN substrate, the team opted to increase the width of the platinum strip from 4mm to approximately 7 mm in order to achieve the desired resistance in fewer coatings. A byproduct of this line of thinking was a platinum strip that aligns more directly with the dimensions of the micro-cooler, which is 10 mm. Based on this, the team believes that increasing the width of the platinum strip and decreasing the thickness may optimize the ratio of cross-sectional area of platinum situated directly above the cooler to volume of the platinum, which would potentially improve cooling rates.

Secondly, experimentation revealed that cooling rates increased as the operating

temperature regime was higher. Based on this, the team recommends continuing to explore the high-temperature functionality of this reactor. Increasing the operating temperature for the given reactor design requires a balance between the heating and cooling capabilities of the reactor given that decreasing the thickness of the film would enhance cooling rates, while increasing the thickness of the film decreases the resistance of the catalyst, allowing for more rapid heating. An alternative to the current design is a platinum strip that is increasingly wide and short in length. This creates lower resistance due to the high width to length ratio as opposed to film thickness, making a thinner coating while still achieving desirable resistances possible. Additionally, this design would allow the reactor to operate as a differential reactor during future gas reaction chemistry, which has documented benefits in heterogeneous catalysis.³³

Finally, the team opted to purchase AlN substrates that were lapped on both sides based on reduced cost and enhanced mechanical adherence of deposited films relative to polished substrates. It is possible; however, that the selection of a lapped substrate may have negatively impacted cooling due to reduced thermal contact. To address this, the team recommends further testing to determine if a substrate that is polished on the bottom side yields more favorable cooling rates. Alternatively, a thermal paste could be applied in between the substrate and the cooling block, although this process would again require additional testing to determine if this would have a positive or negative impact on the reactors heat transfer rates. A final consideration regarding the cooling of the reactor is that the coolant used was ice water. If additional cooling capacity is necessary following the modifications

recommended above, a different coolant could be selected.

6.3 Long-Term Recommendations

6.3.1 Chemical Compatibility

Based on the theory of pulsed catalysis, this methodology should be applicable to other heterogeneous chemical reactions.¹⁹ Therefore, future iterations should consider reactor designs that can be tuned to meet the specific temperature thresholds and oscillation frequencies of other heterogeneously catalyzed reactions.

6.3.2 On-Demand Chemical Manufacturing

If dynamically pulsed catalysis is proven to facilitate higher conversion rates of hydrogen and nitrogen to ammonia at milder reaction conditions, this could revolutionize the chemical manufacturing of ammonia by enabling smaller-scale, decentralized reactor plants, similar to the design proposed in this paper. Opposed to the few massive manufacturers that currently produce the bulk of the world's ammonia, at milder and more energetically favorable reaction conditions, decentralized production facilities would be more economical and could be used for on-demand production. Additionally, further testing of the scalability of thermally pulsed catalysis could prove its efficacy for industrial-scale production.

Appendix A: Final Reactor Component Table

Part	Description	Part #	Qty	Supplier
Reactor Chuck	Aluminum base, machined to reactor specifications	N/A	1	N/A
Internal Union	1/16" internal union, 1/4" hexagonal head	ZU1C	2	VICI
Ferrules (internal union)	1/16" ferrule	ZF1S6-10	2	VICI
Tube Adapters	1/8" to 1/16" tube adapter	B-200-6-1 (Brass) or SS-200-6-1 (316 SS)	2	Swagelok
Gas Flow Tubing	1/16" metal tubing	N/A	2	N/A
Ferrule Set (at gas flow connections)	Set containing 1 front and 1 back 316 stainless steel ferrule	SS-100-SET	2	Swagelok
Cooling Block	Gold plated copper microchannel heatsink	SA-2A	1	Micro Cooling Concepts
Cooling Manifold	Copper	SA-2A (manifold)	1	Micro Cooling Concepts
AlN Chips	0.55x50x16mm AlN substrates, lapped both sides 25u"Ra	27104-3	1	Valley Design Corp.
Pyrometer	Low-temp, high speed, includes pipe adapter and sighting tube	CT 4ML	1	Optris
Window	12.50 x 12.50 ± 0.1, Sapphire	#39-228	1	Edmund Optics

Appendix B: Voltage Heating Complete Data

Voltage (V)	Coolant Flow (mL/min)	Converging Temperature
10	0	31
20	0	64
30	0	123
40	0	204
10	10	28
20	10	58
30	10	116
40	10	194
10	20	24
20	20	55.5
30	20	114
40	20	188
10	30	22
20	30	52.5
30	30	109
40	30	186

Appendix C: Cooling Time and Rate Data

T1	T2	Coolant Flow (mL/min)	Time (s)
100	50	0	0.4579
150	100	0	0.2073
200	100	0	0.3928
250	150	0	0.2996
300	200	0	0.2537
100	50	10	0.3915
150	100	10	0.1955
200	100	10	0.3637
250	150	10	0.2714
300	200	10	0.2212
100	50	20	0.3476
150	100	20	0.1864
200	100	20	0.3487
250	150	20	0.2662
300	200	20	0.2207
100	50	30	0.3628
150	100	30	0.1903
200	100	30	0.3519
250	150	30	0.2698
300	200	30	0.2255

References

- (1) *Mineral Commodity Summaries 2022*; Mineral Commodity Summaries; USGS Numbered Series 2022; U.S. Geological Survey: Reston, VA, 2022; Vol. 2022, p 202. <https://doi.org/10.3133/mcs2022>.
- (2) Nørskov, J.; Chen, J.; Miranda, R.; Fitzsimmons, T.; Stack, R. *Sustainable Ammonia Synthesis – Exploring the Scientific Challenges Associated with Discovering Alternative, Sustainable Processes for Ammonia Production*; 1283146; 2016; p 1283146. <https://doi.org/10.2172/1283146>.
- (3) Round-Trip Efficiency of Ammonia as a Renewable Energy Transportation Media – Ammonia Energy Association.
- (4) Kyriakou, V.; Garagounis, I.; Vourros, A.; Vasileiou, E.; Stoukides, M. An Electrochemical Haber-Bosch Process. *Joule* **2020**, *4* (1), 142–158. <https://doi.org/10.1016/j.joule.2019.10.006>.
- (5) Armstrong, C. D.; Teixeira, A. R. Advances in Dynamically Controlled Catalytic Reaction Engineering. *React. Chem. Eng.* **2020**, *5* (12), 2185–2203. <https://doi.org/10.1039/D0RE00330A>.
- (6) Stolte, J.; Özkan, L.; Thüne, P. C.; Niemantsverdriet, J. W.; Backx, A. C. P. M. Pulsed Activation in Heterogeneous Catalysis. *Appl. Therm. Eng.* **2013**, *57* (1), 180–187. <https://doi.org/10.1016/j.applthermaleng.2012.06.035>.
- (7) Haber, F. The Synthesis of Ammonia from Its Elements Nobel Lecture, June 2, 1920. *Resonance* **2002**, *7* (9), 86–94. <https://doi.org/10.1007/BF02836189>.
- (8) Liu, H. Ammonia Synthesis Catalyst 100 Years: Practice, Enlightenment and Challenge. *Chin. J. Catal.* **2014**, *35* (10), 1619–1640. [https://doi.org/10.1016/S1872-2067\(14\)60118-2](https://doi.org/10.1016/S1872-2067(14)60118-2).
- (9) Humphreys, J.; Lan, R.; Tao, S. Development and Recent Progress on Ammonia Synthesis Catalysts for Haber–Bosch Process. *Adv. Energy Sustain. Res.* **2021**, *2* (1), 2000043. <https://doi.org/10.1002/aesr.202000043>.
- (10) Appl, M. Ammonia, 2. Production Processes. In *Ullmann's Encyclopedia of Industrial Chemistry*; American Cancer Society, 2011. https://doi.org/10.1002/14356007.o02_o11.
- (11) Stoltze, P.; Nørskov, J. K. Bridging the “Pressure Gap” between Ultrahigh-Vacuum Surface Physics and High-Pressure Catalysis. *Phys. Rev. Lett.* **1985**, *55* (22), 2502–2505. <https://doi.org/10.1103/PhysRevLett.55.2502>.
- (12) Ertl, G. Surface Science and Catalysis—Studies on the Mechanism of Ammonia Synthesis: The P. H. Emmett Award Address. *Catal. Rev.* **1980**, *21* (2), 201–223. <https://doi.org/10.1080/03602458008067533>.
- (13) Honkala, K.; Hellman, A.; Remediakis, I. N.; Logadottir, A.; Carlsson, A.; Dahl, S.; Christensen, C. H.; Nørskov, J. K. Ammonia Synthesis from First-Principles Calculations. *Science* **2005**, *307* (5709), 555–558. <https://doi.org/10.1126/science.1106435>.
- (14) Hellman, A.; Baerends, E. J.; Biczysko, M.; Bligaard, T.; Christensen, C. H.; Clary, D. C.; Dahl, S.; van Harrevelt, R.; Honkala, K.; Jonsson, H.; Kroes, G. J.; Luppi, M.; Manthe, U.; Nørskov, J. K.; Olsen, R. A.; Rossmeisl, J.; Skúlason, E.; Tautermann, C. S.; Varandas, A. J. C.; Vincent, J. K. Predicting Catalysis: Understanding Ammonia Synthesis from First-

- Principles Calculations. *J. Phys. Chem. B* **2006**, *110* (36), 17719–17735. <https://doi.org/10.1021/jp056982h>.
- (15) Spencer, M. S. On the Rate-Determining Step and the Role of Potassium in the Catalytic Synthesis of Ammonia. *Catal. Lett.* **1992**, *13* (1), 45–53. <https://doi.org/10.1007/BF00770946>.
- (16) Vojvodic, A.; Medford, A. J.; Studt, F.; Abild-Pedersen, F.; Khan, T. S.; Bligaard, T.; Nørskov, J. K. Exploring the Limits: A Low-Pressure, Low-Temperature Haber–Bosch Process. *Chem. Phys. Lett.* **2014**, *598*, 108–112. <https://doi.org/10.1016/j.cplett.2014.03.003>.
- (17) Ichikawa, S. Volcano-Shaped Curves in Heterogeneous Catalysis. *Chem. Eng. Sci.* **1990**, *45* (2), 529–535. [https://doi.org/10.1016/0009-2509\(90\)87039-U](https://doi.org/10.1016/0009-2509(90)87039-U).
- (18) Logadottir, A.; Rod, T. H.; Nørskov, J. K.; Hammer, B.; Dahl, S.; Jacobsen, C. J. H. The Brønsted–Evans–Polanyi Relation and the Volcano Plot for Ammonia Synthesis over Transition Metal Catalysts. *J. Catal.* **2001**, *197* (2), 229–231. <https://doi.org/10.1006/jcat.2000.3087>.
- (19) Ardagh, M. A.; Abdelrahman, O. A.; Dauenhauer, P. J. Principles of Dynamic Heterogeneous Catalysis: Surface Resonance and Turnover Frequency Response. *ACS Catal.* **2019**, *9* (8), 6929–6937. <https://doi.org/10.1021/acscatal.9b01606>.
- (20) Kalz, K. F.; Kraehnert, R.; Dvoyashkin, M.; Dittmeyer, R.; Gläser, R.; Krewer, U.; Reuter, K.; Grunwaldt, J.-D. Future Challenges in Heterogeneous Catalysis: Understanding Catalysts under Dynamic Reaction Conditions. *ChemCatChem* **2017**, *9* (1), 17–29. <https://doi.org/10.1002/cctc.201600996>.
- (21) IR thermometer for low temperatures on metals: CTlaser 4M <https://www.optris.com/ctlaser-4m> (accessed 2022 -04 -07).
- (22) UV Windows - IR Windows - Ultraviolet Windows - Infrared Windows <https://www.edmundoptics.com/c/ultraviolet-uv-infrared-ir-windows/670/> (accessed 2022 -04 -07).
- (23) Tilli, M.; Haapalinn, A. Chapter 1 - Properties of Silicon. In *Handbook of Silicon Based MEMS Materials and Technologies (Second Edition)*; Tilli, M., Motooka, T., Airaksinen, V.-M., Franssila, S., Paulasto-Kröckel, M., Lindroos, V., Eds.; Micro and Nano Technologies; William Andrew Publishing: Boston, 2015; pp 3–17. <https://doi.org/10.1016/B978-0-323-29965-7.00001-4>.
- (24) The Thermal Conductivity of Silicon Dioxide. *Electronics Cooling*, 2004.
- (25) CeramTec-Rubalit-710-Alumina-996.Pdf.
- (26) Clear fused quartz GE 124, 100mm wafers from stock by Valley. <https://valleydesign.com/GE124-properties.htm> (accessed 2022 -04 -19).
- (27) Aluminum Nitride Lapping Services, ALN Substrates & Wafers <http://aluminumnitride.com/> (accessed 2022 -04 -19).
- (28) Silicon Carbide SiC Material Properties <https://accuratus.com/silicar.html> (accessed 2022 -04 -19).
- (29) The General Properties of Si, Ge, SiGe, SiO₂ and Si₃N₄. 5.
- (30) Aluminum Nitride | AlN Material Properties <https://accuratus.com/alumni.html> (accessed 2022 -04 -19).

- (31) Solvent Clean | McGill Nanotools - Microfab
<http://mnm.physics.mcgill.ca/content/solvent-clean> (accessed 2022 -04 -06).
- (32) Pereira, R.; Marchesi, L. F.; Freitas, R. G.; Matos, R.; Pereira, E. C. A Low-Cost Platinum Film Deposited Direct on Glass Substrate for Electrochemical Counter Electrodes. *J. Power Sources* **2013**, *232*, 254–257. <https://doi.org/10.1016/j.jpowsour.2013.01.040>.
- (33) Ajmera, S. K.; Delattre, C.; Schmidt, M. A.; Jensen, K. F. Microfabricated Differential Reactor for Heterogeneous Gas Phase Catalyst Testing. *J. Catal.* **2002**, *209* (2), 401–412. <https://doi.org/10.1006/jcat.2002.3584>.